Dynamics of Spaetzle morphogen shuttling in the *Drosophila* embryo shapes pattern

Neta Rahimi*, Inna Averbukh*, Shari Carmon, Eyal D. Schejter, Naama Barkai[&] and Ben-Zion Shilo[&#]

Department of Molecular Genetics, Weizmann Institute of Science, Rehovot 76100, Israel

* Equal contribution

[&] Corresponding authors

Lead contact

Abstract

Establishment of morphogen gradients in the early *Drosophila* embryo is challenged by a diffusible extracellular milieu, and rapid nuclear divisions that occur at the same time. To understand how a sharp gradient is formed within this dynamic environment, we followed the generation of graded nuclear Dorsal (Dl) protein, the hallmark of pattern formation along the dorso-ventral axis, in live embryos. We show that a sharp gradient is formed through extracellular, diffusion-based morphogen shuttling that progresses through several nuclear divisions. Perturbed shuttling in *wntD* mutant embryos results in a flat activation peak and aberrant gastrulation. Re-entry of Dl into the nuclei at each cycle refines the signaling output, by guiding graded accumulation of the *T48* transcript that drives patterned gastrulation. We conclude that diffusion-based ligand shuttling, coupled with dynamic readout, establishes a refined pattern within the diffusible environment of early embryos.

Introduction

The crude onset and subsequent refinement of spatial information shapes the future body pattern of embryos. Morphogens, key instructive elements in this context, are secreted signaling molecules that induce cells to adapt different fates depending on their concentration. Establishing a morphogen gradient over a field of naïve cells patterns the cell layer into distinct domains of gene expression (Green and Sharpe, 2015; Wolpert, 1971). Different strategies to guide morphogen distribution have been identified. A common option is to produce the morphogen in a restricted group of cells, giving rise to its graded distribution in the surrounding cells (Lecuit et al., 1996; Nellen et al., 1996). Notably, in this scenario, the morphogen-producing cells are distinct from the responding cells.

An alternative strategy of morphogen distribution is applicable to situations where the morphogen is broadly expressed, and the gradient is generated *within* the field of expressing cells, which also respond to the morphogen. This scenario is applicable to early embryos, where broad transcriptional domains have been established, but have not yet given rise to the determination of sufficiently restricted groups of cells, which could provide a local morphogen source. In such situations, restricting morphogen signaling to a narrow domain becomes a challenge, as diffusion tends to spread, rather than restrict ligand distribution.

Studies in several systems identified the *Shuttling* mechanism as a robust solution to this challenge (Shilo et al., 2013). Here, a morphogen gradient is established not merely by its diffusion away from the production source, but through an effective translocation of the morphogen into the center of the field. This translocation, which is purely diffusion driven, is mediated by a proximally-produced inhibitor. The resulting gradient is sharp and robust, displaying limited sensitivity to gene dosages or reaction rate constants. Shuttling provides robustness by concentrating the morphogen into restricted domain, which allows storing excess levels in regions of maximal signaling without modifying the resulting cell fates. Such a shuttling mechanism establishes the bone morphogenetic protein (BMP) morphogen gradient in the early embryos of *Drosophia* and other insects (Eldar et al., 2002; Lapraz et al., 2009; Shimmi et al., 2005; van der Zee et al., 2006; Wotton et al., 2017). It is also used for forming

54 the BMP gradient in the *Xenopus* embryo, where it acquired additional features that allow
55 scaling of the gradient with embryo size (Ben-Zvi et al., 2014; Ben-Zvi et al., 2008).

56 Compelling evidence for shuttling was provided by comparing mutant phenotypes with the
57 predictions made by computational models (Ben-Zvi et al., 2008; Eldar et al., 2002; Haskel-
58 Ittah et al., 2012). It was also demonstrated that ligand produced ectopically in one part of the
59 embryo can be translocated to and endocytosed in the normal activation domain (Reversade
60 and De Robertis, 2005; Wang and Ferguson, 2005). Experimentally, these data were obtained
61 through the analysis of fixed embryos. Yet, the essence of the shuttling mechanism resides in
62 its *dynamics*. What is the time-frame during which the gradient is established? How fast is
63 gradient formation relative to its readout? Is the gradient stably formed, or is it subject to
64 subsequent cycles of refinements? Insight into these questions requires monitoring the dynamic
65 distribution of the morphogen within single embryos.

66 Furthermore, the shuttling mechanism makes a number of counter-intuitive predictions
67 regarding the dynamics of pattern formation. In particular, it predicts that signaling at the edge
68 of the source will initially increase, as ligand begins to accumulate, but will subsequently be
69 reduced, since ligand is continuously being shuttled to the center of the field. This non-
70 monotonic behavior is a defining property of the shuttling mechanism that concentrates ligand,
71 but is absent from other diffusion-based mechanisms establishing a graded pattern. In a certain
72 parameter range, shuttling also predicts transient formation of a double-peak pattern within the
73 gradient, again a prediction that is absent from naïve gradient-forming mechanisms.
74 Uncovering such features is again possible only by monitoring the dynamics of gradient
75 formation in live embryos.

76 The ability to observe the dynamics of morphogen gradient formation is challenging. The
77 ligands typically function at low levels. Furthermore, the morphogen may be present not only
78 in its active form, but also in a non-processed, inactive form, or bound to an inhibitor. Finally,
79 the morphogen is present in both extra- and intra-cellular locations. Most studies therefore
80 follow the patterning processes by quantifying the intracellular outcome of morphogen
81 signaling as a proxy for active morphogen distribution, using antibodies against the activated
82 (e.g, phosphorylated) states of signaling pathways triggered by morphogens (Dorfman and

83 Shilo, 2001; Gabay et al., 1997; Tanimoto et al., 2000). Such approaches, however, cannot be
84 used to follow live embryos as they rely on immunostaining of fixed samples. An alternative is
85 to follow the transcriptional outcomes of morphogen signaling, but this analysis is already
86 quite removed from the original morphogen gradient itself, and is compounded by additional
87 regulatory inputs controlling the expression of the target genes.

88 Pattering the dorso-ventral (D-V) axis of the *Drosophila* embryo provides a powerful system to
89 analyze the dynamics of morphogen gradient formation. The early *Drosophila* embryo is a
90 syncytium, that is, a collection of nuclei that occupy a common cytoplasm enclosed by the
91 embryonic plasma membrane. Within this syncytium, the nuclei undergo 13 rapid and
92 synchronous divisions without any change in embryo size or shape. During the final four
93 division cycles, the nuclei form a monolayer just beneath the plasma membrane. Spaetzle (Spz)
94 is secreted from the syncytium into the surrounding peri-vitelline fluid, positioned between the
95 plasma and vitelline membranes, and a gradient of active Spz forms within it, along the radial
96 D-V axis. The processed Spz morphogen binds the transmembrane Toll receptor (DeLotto and
97 DeLotto, 1998; Morisato and Anderson, 1994; Schneider et al., 1994; Weber et al., 2003), and
98 triggers Dorsal (Dl) translocation into the syncytial nuclei (Figure 1A). The processed form of
99 the Spz ligand therefore functions as the morphogen at this stage.

100 We previously showed that graded active Spz distribution is established by a shuttling
101 mechanism. In this case, shuttling is implemented in a self-organized manner through a
102 complex interplay between the active ligand and its pro-domain, which can accommodate
103 diverse structures (Haskel-Ittah et al., 2012; Shilo et al., 2013). The resulting gradient of active
104 Spz is sharp, and provides robustness to a variety of perturbations in the level of pathway
105 components.

106 Entry of Dl into the nuclei can be followed in single live embryos carrying a Dl-GFP fused
107 protein (DeLotto et al., 2007). In this work, we use Light Sheet fluorescence microscopy for
108 live imaging of Dl-GFP nuclear localization during the final nuclear division cycles of the
109 syncytial *Drosophila* embryo. The resulting dynamics shows the two signatures of ligand
110 shuttling: a transient increase in signaling in the lateral regions, which is then reduced so as to
111 preferentially increase signaling at the ventral midline, and the resolution of two lateral peaks

112 to a single central peak. We find that ligand shuttling is an ongoing process, which repeats
113 itself following each nuclear division. During the beginning of nuclear cycle (NC) 14, the
114 resulting dynamics of nuclear re-entry of Dl allows to further refine the resulting spatial
115 pattern, by triggering different temporal onsets of zygotic target gene expression in closely
116 positioned nuclei, thereby leading to a functionally significant graded accumulation of target
117 gene transcripts. In *wntD* mutant embryos, the Dl peak becomes flattened, and leads to an
118 abnormal increase in the number of cells simultaneously undergoing the initial step of
119 gastrulation, underscoring the significance of timely and properly shaped gradient formation.
120 Thus, diffusion-based ligand shuttling, coupled with a dynamic readout, establishes a
121 refined pattern within the environment of early embryos.
122

123 # Results

124 **Temporal evolution of the Spz gradient during nuclear cycles 12-14**

125 Using Light Sheet fluorescence microscopy, we followed individual embryos carrying a Dl-
126 GFP fusion protein expressed under the endogenous *Dl* promoter (Figure 1B, SI: movie 1).
127 Consistent with previous reports (DeLotto et al., 2007; Kanodia et al., 2009), we observed a D-
128 V gradient of nuclear Dl-GFP already at NC 12. This gradient was further refined and
129 elaborated during the next two cycles. To enable quantitative analysis of Dl-GPF nuclear
130 dynamics, we used an area preserving transformation to project the 3D images onto a 2D sheet.
131 We restricted our analysis to a region surrounding the A-P midline, where distortion due to 2D
132 projection is negligible (Figure 1C, SI: movie 2) (Heemskerk and Streichan, 2015). Next, we
133 automatically segmented the nuclei and averaged the nuclear Dl-GFP signal in nuclei
134 occupying a similar D-V axis position.

135 Our measurements defined the quantitative, spatio-temporal dynamics of Dl-GFP at a 1-2
136 minute time resolution (Figure 1C-D, SI: movie 3, Methods). This dynamics results from the
137 extracellular active Spz gradient. However, inferring the profile of this extracellular gradient
138 from Dl-GFP dynamics is confounded by the fact that Dl-nuclear accumulation is established
139 anew at every nuclear cycle, since Dl exits the nucleus at mitosis upon nuclear envelope

140 breakdown. We therefore needed a framework to suitably infer properties of the extracellular
141 active Spz gradient, and critically distinguish between models of gradient formation.

142 Toll signaling, at each given position along the D-V gradient, triggers the level of nuclear Dl
143 and the rate by which this level increases. Thus, at the beginning of each division cycle,
144 following re-establishment of the nuclear envelope, nuclear Dl levels increase at a rate that is
145 proportional to the level of nearby Toll signaling. Conversely, at longer times, nuclear Dl
146 levels approach a steady state, and are proportional to the extracellular Toll signaling. We
147 therefore plotted the dynamics of both parameters, nuclear Dl levels and its temporal change
148 during the onset of NC 14. Notably, we observe that this qualitative dynamics differs,
149 depending on the spatial position of nuclei along the D-V axis. In the ventral-most regions they
150 increased monotonically. In contrast, in lateral domains nuclear Dl displayed an overshoot,
151 initially increasing but then starting to decrease (Figure 2A-D, Figure S1). Clearly, such a
152 decrease in nuclear Dl is only possible if Toll signaling at this position decreases as well.
153 Therefore, the data indicates that the external Spz gradient continues to evolve through the
154 early part of NC 14, showing a distinct position-dependent, non-monotonic temporal signature.

155 To more rigorously infer dynamic properties of the external gradient from the measured pattern
156 of nuclear Dl, we used computer simulations, modeling Dl-nuclear entry while assuming
157 different temporal patterns of Toll signaling (Figure 2E-L). Specifically, we searched for a
158 qualitative signature that distinguishes between three scenarios: (1) constant Toll signaling; (2)
159 Toll signaling that is changing (increasing) monotonically in time, as expected in naïve
160 gradient-forming models; and (3) a non-monotonic increase in Toll signaling, the signature
161 found in lateral regions of gradients formed by the shuttling mechanism. Our simulations have
162 shown that these scenarios are best distinguished by comparing the temporal changes in
163 nuclear Dl (d(Dl)/dt) with the levels of nuclear Dl. In the first two cases – constant or
164 monotonically increasing Toll activity – the relation between these two parameters is
165 invariably linear or concave (Figure 2E-L). In contrast, in the presence of non-monotonic
166 shuttling-based dynamics, a convex relation is obtained, with a pronounced negative temporal
167 derivative at the lateral regions, where nuclear Dl levels are low (Figure 2M-P).

168 The measured data is not consistent with the dynamic defined by constant, or monotonically
169 increasing Toll signaling. Rather, it shows a clear signature of non-monotonic, shuttling-like
170 dynamics. Extending our simulations to include the full shuttling model that establishes the
171 active Spz gradient combined with Dl nuclear transport (See SI), confirmed that this model is
172 fully capable of simulating the experimentally observed dynamics, including the non-
173 monotonic, overshoot dynamics at the lateral regions.

174 An additional notable property of Dl-nuclear entry dynamics was the initial formation, at every
175 nuclear cycle, of two ventro-lateral signaling peaks, that eventually converge to a single ventral
176 peak (Figures 1D, 2A, Figure S1). Thus, by 10-15 minutes into NC 14, when the major target
177 genes for Dl are induced, the initial two-peak gradient has refined to a single sharp peak. The
178 initial two-peak pattern provides another unique signature of shuttling-like dynamics. It is
179 expected under certain shuttling parameters, when the mean distance traveled by the shuttling
180 complex before it is cleaved, is much smaller than the distance to the ventral-most site. In this
181 case, ligand will initially accumulate at lateral regions, followed by gradual ventral
182 translocation (See SI). The reappearance of the double peak at every nuclear cycle likely
183 reflects a process of extracellular ligand mixing in the peri-vitelline fluid, possibly caused by
184 reorganization of the cortical actin-based cytoskeleton and deformation of the plasma
185 membrane associated with the nuclear divisions (di Pietro and Bellaiche, 2018; Zhang et al.,
186 2018).

187 In conclusion, the dynamic behavior of Dl-GFP supports a continuous process of extracellular
188 Spz shuttling, displaying two of its defining signatures: non-monotonic dynamics of nuclear Dl
189 entry in lateral regions, and the transient formation of two-peak gradient.

190 **Altered shuttling dynamics in *wntD* mutants affects gastrulation**

191 Dl-nuclear localization dynamics can be used for refined analysis of informative mutant
192 phenotypes. We applied this approach to study WntD, an inhibitor of Toll signaling which
193 provides a negative feedback that buffers the D-V patterning gradient against fluctuations
194 (Rahimi et al., 2016). *wntD*, a target of the Toll pathway, is transcribed locally at the posterior

195 terminus of the embryo, and the secreted protein diffuses within the peri-vitelline fluid to
196 attenuate Toll signaling (Figure 3A)(Helman et al., 2012).

197 Genetic epistasis experiments have demonstrated that WntD binds the Frizzled-4 (Fz4)
198 receptor, and associates with the extracellular domain of Toll (Rahimi et al., 2016)(Figure 3B).
199 However, the consequences of this inhibition on gradient formation remained unclear. One
200 option is that WntD uniformly decreases signaling in all regions. Alternatively, with the
201 shuttling mechanism in mind, our simulations suggested that the binding of WntD to the
202 extracellular domain of Toll promotes ligand shuttling. This is because the binding of WntD to
203 the Toll receptor decreases the number of available receptors. This, in turn, compromises the
204 ability of free Spz to bind Toll, thereby increasing the probability that it will bind the free
205 shuttling molecule. Binding of Spz to Toll will thus be directed to more ventral regions, where
206 the levels of the shuttling molecules are sufficiently low. Uniform distribution of moderate
207 WntD levels would therefore lead to redistribution of the ligand to more ventral regions,
208 impacting not only on the strength of Toll signaling, but also on its sharpness (see Figure 3C,F
209 for simulation results).

210 Using live imaging in a *wntD* mutant background, we directly tested the possibility that WntD
211 promotes shuttling. Indeed, in *wntD* mutant embryos shuttling was less efficient. First, the
212 initial signature of a double peak was more prominent and persistent. Second, in contrast to *wt*
213 embryos where gradual sharpening of the gradient takes place, in a *wntD*-mutant background
214 the final gradient was relatively wide and displayed a flattened single peak (Figures 3C-J, S2)
215 – consistent with the predicted role of WntD in redistribution of the Spz ligand (Figure 3K-L).

216 To follow the morphological consequences of a wider peak distribution of nuclear Dl
217 distribution, we monitored *wntD* mutant embryos for an extended period of NC 14, observing
218 the processes of gastrulation and ventral furrow formation. We defined the edges of the
219 furrowing domain by marking the two lateral-most nuclei that alter their orientation upon
220 gastrulation. Working backwards to an earlier phase of NC 14, when the nuclei are still in a
221 monolayer, we can accurately count the number of nuclei between these edges. In contrast to
222 gastrulating *wt* embryos where the initial invagination is observed in ~9 cells, in *wntD* mutants
223 a broader front of up to 15 cells invaginated at the same time (Figure 4). Thus, the shape of the

224 Dl-activation gradient is essential for normal patterning and gastrulation. When the final
225 gradient peak is not sharp, a larger cohort of ventral cells takes part in furrow formation.

226 **Timing of *wntD* transcription**

227 *wntD* mutants display perturbed Dl dynamics already at NC 13 (Figures 3H, S3) suggesting
228 that WntD normally exerts its modulating effects at this early stage. This implies that zygotic
229 expression of *wntD*, its translation, secretion to the peri-vitelline fluid and diffusion of the
230 protein, have commenced by then. To examine that this is possible, we applied our Light
231 Sheet-based visualization setup as a more sensitive assay for defining the onset and temporal
232 dynamics of *wntD* expression.

233 *wntD* expression is activated by nuclear Dl, and is restricted to the posterior region, where
234 Torso signaling relieves Capicua (Cic) repression (Helman et al., 2012). We generated a
235 *wntD*::MS2 reporter, utilizing the genomic upstream regulatory sequence of *wntD* (Figure 5A).
236 The early expression profile of the reporter at the posterior part of the embryo mimics the
237 known pattern of *wntD* (Rahimi et al., 2016). Importantly, all eight embryos examined
238 expressed *wntD*, implying that overshooting of Toll signaling, which triggers expression of the
239 WntD "buffer", is a common consequence of D-V gradient signaling. When monitoring the
240 dynamics of *wntD* expression, the number of active nuclei transcribing *wntD* decreased
241 continuously between NCs 12 and 14 (Figure 5B-F). These results suggest that the WntD
242 protein already exerts its attenuating effect on Toll signaling at an early time.

243 **Dl nuclear re-entry promotes graded expression of the zygotic *T48* gene by different**
244 **temporal onsets of transcription**

245 The gradient of Dl-nuclear localization defines three major domains of zygotic gene expression
246 along the D-V axis. Within each of these domains several target genes are uniformly
247 expressed. The mesoderm is defined by highest levels of nuclear Dl and uniform expression of
248 the zygotic target genes *twist* (*twi*) and *snail* (*sna*) (Rusch and Levine, 1996). However, a
249 graded zygotic response within the mesoderm is also required: A gradient of apical myosin II
250 recruitment, peaking at the ventral midline, is essential for the ordered apical cell constriction
251 driving ventral furrow formation (Heer et al., 2017). A zygotic target gene that may lead to

252 graded myosin II distribution is *T48*, since the T48 protein recruits Rho GEF2 to the apical
253 membrane, triggering the accumulation and contractile activity of an apical actomyosin
254 network (Kolsch et al., 2007). We asked whether the dynamics of Dl-nuclear entry may play a
255 role in generating a graded transcriptional response within this region, by following the zygotic
256 target gene *T48.*

257 Previous analysis of an MS2 reporter for *T48* transcription demonstrated that the ventral-most
258 nuclei initiate transcription earlier than the lateral ones (Lim et al., 2017). Using the same
259 reporter, we find that signal intensity in transcribing nuclei is similar regardless of their
260 position along the D-V axis, suggesting that once *T48* transcription is initiated, it progresses at
261 a constant rate in all nuclei (Figure 6C). If zygotic expression of Dl-target genes depends not
262 only on the final, steady-state level of nuclear Dl, but also on the dynamic profile of its
263 accumulation, the signaling output could be further sharpened. A dynamic phase of Dl nuclear
264 entry takes place during the initial 20 minutes of NC 14 (Figure 1D), the nuclear cycle
265 associated with a major onset of zygotic gene expression. A consequence of these dynamics is
266 that ventral-most nuclei will reach the threshold for expression of a given zygotic gene earlier
267 than more lateral ones. These ventral nuclei will begin to express the gene earlier, therefore
268 expressing it for a longer period than more lateral nuclei, and could thus accumulate more
269 transcripts.

270 To examine the consequences of the graded onset of *T48* transcription on mRNA
271 accumulation, we carried out quantitative single-molecule FISH using *T48* probes. The signal
272 obtained is comprised of two components: Prominent puncta in the nuclei representing active
273 transcription of the gene, and sparse weaker spots in the cytoplasm marking accumulated
274 individual mRNA molecules. We analyzed embryos that demonstrated ongoing transcription in
275 several nuclear rows along the D-V axis. The number of transcribing nuclei in ventral and
276 lateral positions within the expression domain was similar, and the transcription intensity in the
277 different rows appears comparable. This again indicates that once *T48* transcription is initiated,
278 it progresses at a constant rate in all nuclei, regardless of position (Figure 6D-E). We next
279 quantitated the levels of cytoplasmic *T48* mRNA, using the TransQuant (Bahar Halpern and
280 Itzkovitz, 2016). A clear D-V gradient of cytoplasmic mRNA accumulation is observed across
281 several cell rows, peaking at the ventral midline (Figure 6F-G). This result indicates that the

282 *T48* mRNA is sufficiently stable during the temporal window of early NC 14, such that the
283 time of onset of its transcription along the D-V axis, governed by the dynamics of Dl nuclear
284 entry, correlates with the level of mRNA that accumulates in the adjacent cytoplasm. Dl
285 nuclear entry dynamics thus appear to be a critical factor regulating graded *T48* activity along
286 the D-V axis.

287 # Discussion

288 **Dynamics of the Spz extracellular morphogen gradient**

289 The early *Drosophila* embryo provides extreme challenges for the generation and maintenance
290 of extracellular morphogen gradients. Most notably, the peri-vitelline fluid surrounding the
291 embryo facilitates rapid diffusion of molecules (Stein et al., 1991). In addition, the alteration in
292 the surface of the plasma membrane at every nuclear division provides an active mixing force
293 (di Pietro and Bellaiche, 2018; Zhang et al., 2018). Thus, analysis of the early morphogen
294 gradients operating in this environment, including ventral Spz/Toll activation and the
295 subsequent BMP gradient patterning the dorsal aspect, should consider this highly dynamic
296 environment. In the case of the Toll pathway, the active Spz ligand is generated by proteolytic
297 processing within the extra-embryonic peri-vitelline fluid in a broad ventral region, defined by
298 the activation domain of the Easter (Ea) protease (Cho et al., 2012). The generation of a sharp
299 Spz activation gradient within this broad ventral domain of processing takes place by
300 diffusion-based shuttling. Our previous work demonstrated that the pro-domain of Spz plays an
301 instructive role in delivering the active, cleaved ligand towards the ventral midline (Haskel-
302 Ittah et al., 2012). While a variety of experiments and computational analyses indicated the
303 utilization of a "self-organized shuttling" mechanism in this context, it was imperative to
304 visualize the actual dynamics of the process.

305 We were able to infer the dynamics of the extracellular Spz gradient by following the kinetics
306 of Dl-GFP nuclear accumulation in individual live embryos during the final syncytial nuclear
307 division cycles and the early phase of NC 14. Nuclear levels of Dl are not a direct readout of
308 the extracellular gradient, since accumulation of Dl in the nuclei is re-initiated at the onset of
309 every nuclear cycle. Nevertheless, it is possible to infer key features of the extracellular Spz

310 gradient from this dynamic behavior. Using this approach we identified clear hallmarks of
311 ligand shuttling, most notably the lateral overshoot and the presence of two lateral peaks which
312 converge to a central ventral peak. This convergence takes place within a timeframe of
313 minutes, and repeats at every nuclear cycle. Since new protein molecules of the extracellular
314 components are continually translated, the ongoing activity of the shuttling process is vital.
315 Therefore, shuttling is important not only for generating the gradient, but also for maintaining
316 it, in the face of rapid diffusion and mixing within the peri-vitelline fluid. Importantly, by ~10-
317 15 minutes into NC 14, when the robust induction of transcription of the cardinal zygotic Dl-
318 target genes *twt* and *sna* ensues, the nuclear gradient of Dl is sharp and a single ventral peak is
319 resolved.

320 **The role of WntD in shaping and buffering the Spz gradient**

321 Having described the dynamics of Dl-nuclear entry and gradient formation, we were in a
322 position to use our experimental approach in order to examine regulatory processes affecting
323 Toll signaling. The Wnt family ligand WntD provides an essential buffering system to
324 variations in Toll signaling between embryos (Rahimi et al., 2016). *wntD* is an early zygotic
325 gene that is expressed initially at the posterior-ventral region of the embryo, and its expression
326 levels depend on the magnitude of Toll signaling (Helman et al., 2012). Although WntD is
327 produced locally, the rapid secretion and diffusion of the protein in the peri-vitelline space
328 generates a uniform attenuation of Toll signaling throughout the embryo surface. The activity
329 of WntD leads in different embryos to convergence of the variable global Toll activation
330 gradient to a similar pattern, which is dictated by the fixed final signaling level that shuts off
331 *wntD* expression (Rahimi et al., 2016). We term this paradigm "distal pinning", achieved in
332 this case by an induction-contraction mechanism (Shilo and Barkai, 2017).

333 Secreted WntD is recruited to the plasma membrane by binding to its receptor Fz4. Epistasis
334 assays have indicated that WntD exerts its inhibitory effect on Toll signaling by associating
335 with the extracellular domain of Toll (Rahimi et al., 2016), thereby reducing the number of
336 Toll receptors that are available for binding Spz. Bearing the cardinal features of shuttling in
337 mind, this mode of inhibition implies that the effect of WntD would be global and non-

338 autonomous, and will actually change the shape of the gradient, making it sharper. The
339 observed dynamics of Dl-GPF in *wntD* mutant embryos indeed confirms this prediction.

340 The shuttling process is driven by competition between the inhibitory Spz pro-domain and the
341 Toll receptor for binding free, active Spz. Binding to the pro-domain is favored in the lateral
342 part of the embryo, where its concentration is higher, while in more ventral regions binding to
343 Toll takes over. Since WntD impinges on the extracellular properties of the Toll receptor, the
344 active ligand is deposited in more ventral regions, where the concentration of the pro-domain is
345 lower. Thus, WntD does not simply reduce the overall profile of Toll activation, but actually
346 *re-directs* the ligand from the lateral regions to the ventral domain. We have previously shown
347 that accumulation of excess ligand in the peak by shuttling is an effective mechanism to buffer
348 noise. Since activation in this region is already maximal, the excess ligand will not alter the
349 resulting cell fates (Barkai and Shilo, 2009).

350 The rapid timing of processes in the early embryo and the short duration of interphases
351 between nuclear divisions raises the question of whether it is actually possible to produce
352 sufficient levels of WntD that will drive the morphogen profile to the desired equilibrium.
353 When monitoring *wntD* transcription directly utilizing the MS2 system, we saw that most, if
354 not all embryos express *wntD*, indicating that Toll signaling overshoots in most embryos.
355 Furthermore, within single embryos the number of nuclei expressing *wntD* was reduced
356 between NCs 12 and 13, and completely terminated by NC 14, implying that WntD impinges
357 on the Toll gradient and its own expression by this time. The intronless arrangement of the
358 *wntD* gene and the rapid secretion of the protein, which does not require post-translational
359 modifications (Herr et al., 2012), may facilitate the process.

360 **Dl nuclear re-entry refines its signaling output**

361 The ventral cohort of zygotic target genes including *twi* and *sna* is induced by the Toll
362 activation gradient, and the threshold for their induction corresponds to ~50% of maximal Dl-
363 nuclear localization (Kanodia et al., 2009; Liberman et al., 2009). Within the ventral domain,
364 nuclei exhibit a similar level of *sna* transcription (Bothma et al., 2015; Lagha et al., 2013).

365 These genes are triggered at NC 14 after the Dl gradient is stabilized and a distinct activation
366 peak generated.

367 Are there zygotic target genes that respond to the dynamics of Dl nuclear targeting, before it
368 stabilizes? This appears to be the case for *T48*, which encodes a transmembrane protein that
369 facilitates recruitment of RhoGEF2 and ultimately Rho and actomyosin, to mediate apical
370 constriction of invaginating mesodermal cells (Kolsch et al., 2007). Graded distribution of
371 myosin II was shown to be critical for proper invagination of these cells to form the ventral
372 furrow (Heer et al., 2017).

373 We provide evidence that the graded distribution of *T48* mRNA results from the dynamics of
374 Dl-nuclear re-entry at NC 14. The ventral-most cells reach the threshold of *T48* induction
375 earlier than more lateral cells, and hence will express the gene longer (Lim et al., 2017).
376 Integration of the length of expression along the D-V axis then leads to a gradient of
377 cytoplasmic *T48* mRNA accumulation. This example represents a unique case, where graded
378 morphogen activation instructs the generation of a gradient of target-gene expression. The
379 strict dependence on the *timing* of transcription initiation provides another mechanism to
380 generate differences between adjacent nuclei along the D-V axis.

381 In conclusion, this work has utilized live imaging of Toll pathway activation, to identify and
382 characterize the hallmarks of ligand shuttling (Figure 7). This process is rapid and takes place
383 continuously throughout the final nuclear division cycles, to generate and maintain a sharp
384 activation gradient in the diffusible environment of the peri-vitelline fluid. WntD impinges on
385 Spz shuttling, and is responsible not only for buffering variability between embryos, but also
386 for generating a sharp activation peak. This peak is utilized to induce a graded expression of a
387 zygotic target gene that is essential for executing processes that drive gastrulation. Thus,
388 diffusion-based ligand shuttling, coupled with a dynamic readout, establishes a refined pattern
389 within the environment of early embryos.
390

391

392

Acknowledgements

We thank B. Lim and M. Levine for the *T48*::MS2 flies, and S. Itskovitz for advice on single-molecule FISH. We are grateful to Y. Addadi and O. Golani for help in acquisition and analysis of Light Sheet images, and S. Streichan for support in 3D image processing. Imaging using the Light Sheet microscope was made possible thanks to The de Picciotto-Lesser Cell Observatory in memory of Wolf and Ruth Lesser. We thank the members of the Shilo and Barkai labs for fruitful discussions. The work was supported by an ERC advanced grant to N.B. and a US-Israel Binational grant to E.S. and B.S. B.S. is an incumbent of the Hilda and Cecil Lewis chair in Molecular Genetics.

Methods

Fly stocks and genetics

For the *wt* dlGFP experiments we used Sco/Cyo;*dl-GFP/*Tm3, Sb flies (DeLotto et al., 2007). For the *wntD* mutant background, a recombination between a *wntD* null allele (Rahimi et al., 2016)and *dl-GFP* was carried out, and crossed to *wntD* mutant.

wntD::*MS2-Fhos-RH* generation: the 1162 bp upstream of *wntD* transcription start site were synthesized followed by 24 repeats of the MS2 sequence, and placed within the 5UTR. The sequence was inserted into a pAttB vector with *NotI* and *KpnI* sites. The *Fhos-RH* sequence was further ligated into the *NotI* site to generate *wntD*::MS2-Fhos-RH. Virgin females expressing both MCP::GFP and His:RFP were crossed with males of the reporter line *wntD*::*MS2-Fhos-RH* to collect embryos for imaging.

MCP::GFP and *t4*::*MS2-yellow* fly lines (Lim et al., 2017) used in the quantitative live imaging of *T48* induction were kindly provided by B. Lim. Virgin females carrying both MCP::GFP and His:RFP were crossed with males of the reporter line *T48::MS2-yellow* and embryos collected for imaging.

419 **Live Imaging**

420 Embryos were imaged using a Light Sheet z1 microscope (Zeiss Ltd.) equipped with 2 sCMOS
421 cameras PCO-Edge, 10X excitation objectives and Light Sheet Z.1 detection optics 20×/1.0
422 (water immersion). The embryos were collected, dechorionated and up to 4 embryos were
423 sequentially mounted perpendicularly into a glass capillary (Brand) in a 1% low melting
424 agarose solution (Roth). Imaging was preformed using dual side illumination, zoom X0.8. GFP
425 Excitation: 488nm Emission / detection - BP 505-545, RFP Excitation: 561nm Emission /
426 detection - BP 575-615.

427 The *T48::MS2* expressing embryos were mounted on a cover slide and imaged through
428 halocarbon oil in a Zeiss LSM710 confocal system at a temporal resolution of 3 minutes.

429 **MS2 analysis**

430 MCP-GFP spots were manually counted using the Imaris software after adjusting the contrast
431 min&max for enhanced visualization. In the *T48::MS2* analysis the spots were manually
432 detected and displayed using the Imaris spots object.

433 **sm-FISH**

434 Stellaris RNA FISH probe sets for the *T48* gene (5' UTR and coding, not including the 3'
435 UTR), were designed by Stellaris Probe Designer and purchased from LGC Biosearch
436 Technologies. 3 hrs after egg lay (AEL) *wt* embryos were fixed for 25 min in 4%
437 formaldehyde, washed in Methanol and kept at -20°C. Next day embryos were washed in
438 Methanol and then in Ethanol, rocked in 90% Xylene, 10% Ethanol for 1 hr followed by post
439 fixation. Then incubated 6' with Proteinase K and post fixed again. Embryos were transferred
440 gradually to 10% FA in 2X SSC + 10 µg/ml ssDNA preheated to 37°C and prehybredized for
441 30' at 37°C. Hybridization Buffer included 10% FA, 10% Dextran, 2mg/ml BSA, RVC and
442 ssDNA+ tRNA in 2X SSC, containing the probe set (1 ng/µl) (Trcek et al., 2017).
443 Hybridization was carried out O/N at 37°C. Next morning the embryos were shaken gently and
444 incubated for another 30'. Embryos were washed twice for 30' at 37°C with 10% FA in 2X
445 SSC + 10 µg/ml ssDNA and gradually transferred to PBS-0.5% Tween and mounted with
446 Vectashield+DAPI Mounting Medium (Vector Laboratories Inc.). Fluorescence was visualized

447 with a Nikon Eclipse Ti2 microscope, and analyzed by the TransQuant script as was previously
448 published (Bahar Halpern and Itzkovitz, 2016). TS Intensities were measured via ImageJ.

449 **Light Sheet movies analysis**

450 **Projection to 2D**

451 To enable quantitative analysis of the nuclear Dl gradient, we projected the 3D scans of the
452 embryo from the light-sheet microscope, into a 2D flat surface, for every time point imaged.
453 This was possible, since all the nuclei are arranged on the surface of the embryo, whose shape
454 resembles an ellipsoid. This ellipsoid can be projected into a 2D surface, which contains all the
455 nuclei and therefore the entire nuclear Dl gradient. To this end, we used an area preserving
456 transformation with minimal distortion far from the Anterior and Posterior poles, implemented
457 by the IMSANE tissue cartography tool (Heemskerk and Streichan, 2015). IMSANE was used
458 with the following specifications: Planar Illastik surface detector and cylinder chart type.
459 Surface detection was performed on the last time point for each embryo, and the detected
460 surface was then used to project all earlier time points. Since the embryo is, to a good
461 approximation, a cylinder apart from the anterior and posterior poles, embryo circumference
462 was defined as the largest circumference of the ellipsoid fitted to the embryo surface by
463 IMSANE.

464 **Nuclei segmentation**

465 The nuclei were detected separately for each time point, using the following segmentation
466 method:

467 1. Automated local thresholding of the image in order to create a binary mask. Done
468 in ImageJ using the Bernsen algorithm with a contrast threshold of 15.
469 2. The resulting binary mask underwent further refinement to segment the nuclei
470 using MATLAB image analysis filters:
471 a. All connected objects in the mask large enough to be nuclei (over 50
472 pixels in size) were located and classified into 3 size groups: *small* 50-150
473 pixels, *medium* 150-600 pixels and *large* 600 pixels and over.
474 b. Each size group underwent erosion using *imerode* and then dilation using
475 *imdilate* with appropriate filter sizes for each group.

476 c. Objects belonging to the *large* group underwent another round of erosion
477 and dilation with same filter size as first round.
478 3. The resulting objects in the binary mask were filtered by size to exclude objects
479 too small (under 50 pixels) or too large (over 3000 pixels) to be a single nucleus.
480 4. Nuclei locations were detected by overlaying the mask on the original image.

481 **Measuring the nuclear Dl gradient around the A-P midline**

482 Gradient measurement was performed by first manually discarding all time points between the
483 nuclear cycles. Then, for every detected nucleus, for all remaining time points, the value of
484 nuclear Dl was calculated as the mean intensity inside the nucleus (located by the above
485 segmentation method). The location of the A-P midline was manually selected for each
486 embryo. A rectangular area around the A-P midline was then defined. The width of the area
487 along the A-P axis was 15% of entire A-P length and it spanned the entire D-V axis. For NC14,
488 this definition corresponds to ~8- 10 columns of nuclei closest to the A-P midline. Only the
489 nuclei inside this area were taken into account for gradient measurement, monitoring several
490 columns of nuclei along the A-P axis gave rise to averaging of Dl-nuclear intensity along this
491 small window. The spatial axis for the gradient was defined as a relative axis- x/L, indicating
492 location on the D-V axis- x divided by embryo circumference- L. In order to assign a location
493 on this relative D-V axis for each nucleus, the location of the D-V midline was manually
494 selected and defined as $x/L = 0$. This resulted in the raw intensity function, $Dl_{raw}(x/L, t)$
495 measuring nuclei intensity along the relative D-V axis, over time. This function, $Dl_{raw}(x/L, t)$,
496 was then smoothened **in space, for each time point separately** using the MATLAB *smooth*
497 function with a smoothing coefficient of 0.23. The smoothened data was then fitted by a
498 smoothing spline using the MATLAB *fit* function and evaluated on a 1000 linearly spaced
499 x/L locations. The resulting function, $Dl_{smooth}(x/L, t)$, was plotted in main text figures.

500 **Dorsal gradient as a function of time, at specific locations along the D-V axis**

501 For the calculation of Dl-nuclear intensity over time at a specific location $\tilde{x}/L$, we used
502 $Dl_{smooth}(x/L, t)$ at that location: $Dl_{smooth}(\tilde{x}/L, t)$. Background subtracted values were
503 calculated separately for each NC, by subtracting the minimal intensity observed in a nucleus
504 for that NC. $Dl_{smooth}(\tilde{x}/L, t)$ was then smoothened in time using the MATLAB *smooth*

function with the *loess* method and a smoothing coefficient of 0.5. It was then fitted with a smoothing spline, resulting in the function $Dl_{\tilde{x}/L}^{fitted}(t)$. The temporal derivative of nuclear Dorsal, at a specific location- $\tilde{x}/L$ was calculated by applying a third order finite differences formula to $Dl_{\tilde{x}/L}^{fitted}(t)$ and then smoothing using *smooth* with a smoothing coefficient of 0.6 and fitting a smoothing spline.

Measuring peak sharpness

The peak sharpness measure for an embryo was calculated based on the values of $Dl_{smooth}(x/L, t)$, around the ventral-most location. For each time point, $\tilde{t}$, $Dl_{smooth}(x/L, \tilde{t})$ was normalized by dividing by its maximal value at $\tilde{t}$. Peak sharpness was then calculated as the standard deviation divided by the mean, in percent, of values close to the peak: within the range $\frac{x}{L} \in [-0.1, 0.1]$. This measure captures how different from each other are values close to the peak.

529 # References

530 Bahar Halpern, K., Itzkovitz, S., 2016. Single molecule approaches for quantifying
531 transcription and degradation rates in intact mammalian tissues. Methods 98, 134-142.
532 Barkai, N., Shilo, B.Z., 2009. Robust generation and decoding of morphogen gradients. Cold
533 Spring Harb Perspect Biol 1, a001990.
534 Ben-Zvi, D., Fainsod, A., Shilo, B.Z., Barkai, N., 2014. Scaling of dorsal-ventral patterning in
535 the Xenopus laevis embryo. Bioessays 36, 151-156.
536 Ben-Zvi, D., Shilo, B.Z., Fainsod, A., Barkai, N., 2008. Scaling of the BMP activation gradient
537 in Xenopus embryos. Nature 453, 1205-1211.
538 Bothma, J.P., Garcia, H.G., Ng, S., Perry, M.W., Gregor, T., Levine, M., 2015. Enhancer
539 additivity and non-additivity are determined by enhancer strength in the Drosophila embryo.
540 Elife 4.
541 Cho, Y.S., Stevens, L.M., Sieverman, K.J., Nguyen, J., Stein, D., 2012. A ventrally localized
542 protease in the Drosophila egg controls embryo dorsoventral polarity. Curr Biol 22, 1013-
543 1018.
544 DeLotto, R., DeLotto, Y., Steward, R., Lippincott-Schwartz, J., 2007. Nucleocytoplasmic
545 shuttling mediates the dynamic maintenance of nuclear Dorsal levels during Drosophila
546 embryogenesis. Development 134, 4233-4241.
547 DeLotto, Y., DeLotto, R., 1998. Proteolytic processing of the Drosophila Spatzle protein by
548 easter generates a dimeric NGF-like molecule with ventralising activity. Mech Dev 72, 141-
549 148.
550 di Pietro, F., Bellaiche, Y., 2018. Actin Network Discussion during Mitotic Pseudo-Furrowing.
551 Dev Cell 45, 539-541.
552 Dorfman, R., Shilo, B.Z., 2001. Biphasic activation of the BMP pathway patterns the
553 Drosophila embryonic dorsal region. Development 128, 965-972.
554 Eldar, A., Dorfman, R., Weiss, D., Ashe, H., Shilo, B.Z., Barkai, N., 2002. Robustness of the
555 BMP morphogen gradient in Drosophila embryonic patterning. Nature 419, 304-308.
556 Gabay, L., Seger, R., Shilo, B.Z., 1997. MAP kinase in situ activation atlas during Drosophila
557 embryogenesis. Development 124, 3535-3541.
558 Green, J.B., Sharpe, J., 2015. Positional information and reaction-diffusion: two big ideas in
559 developmental biology combine. Development 142, 1203-1211.
560 Haskel-Ittah, M., Ben-Zvi, D., Branski-Arieli, M., Schejter, E.D., Shilo, B.Z., Barkai, N., 2012.
561 Self-organized shuttling: generating sharp dorsoventral polarity in the early Drosophila
562 embryo. Cell 150, 1016-1028.
563 Heemskerk, I., Streichan, S.J., 2015. Tissue cartography: compressing bio-image data by
564 dimensional reduction. Nat Methods 12, 1139-1142.
565 Heer, N.C., Miller, P.W., Chanet, S., Stoop, N., Dunkel, J., Martin, A.C., 2017. Actomyosin-
566 based tissue folding requires a multicellular myosin gradient. Development 144, 1876-1886.
567 Helman, A., Lim, B., Andreu, M.J., Kim, Y., Shestkin, T., Lu, H., Jimenez, G., Shvartsman,
568 S.Y., Paroush, Z., 2012. RTK signaling modulates the Dorsal gradient. Development 139,
569 3032-3039.
570 Herr, P., Hausmann, G., Basler, K., 2012. WNT secretion and signalling in human disease.
571 Trends Mol Med 18, 483-493.

572 Kanodia, J.S., Rikhy, R., Kim, Y., Lund, V.K., DeLotto, R., Lippincott-Schwartz, J.,
573 Shvartsman, S.Y., 2009. Dynamics of the Dorsal morphogen gradient. Proc Natl Acad Sci U S
574 A 106, 21707-21712.
575 Kolsch, V., Seher, T., Fernandez-Ballester, G.J., Serrano, L., Leptin, M., 2007. Control of
576 Drosophila gastrulation by apical localization of adherens junctions and RhoGEF2. Science
577 315, 384-386.
578 Lagha, M., Bothma, J.P., Esposito, E., Ng, S., Stefanik, L., Tsui, C., Johnston, J., Chen, K.,
579 Gilmour, D.S., Zeitlinger, J., Levine, M.S., 2013. Paused Pol II coordinates tissue
580 morphogenesis in the Drosophila embryo. Cell 153, 976-987.
581 Lapraz, F., Besnardeau, L., Lepage, T., 2009. Patterning of the dorsal-ventral axis in
582 echinoderms: insights into the evolution of the BMP-chordin signaling network. PLoS Biol 7,
583 e1000248.
584 Lecuit, T., Brook, W.J., Ng, M., Calleja, M., Sun, H., Cohen, S.M., 1996. Two distinct
585 mechanisms for long-range patterning by Decapentaplegic in the Drosophila wing. Nature 381,
586 387-393.
587 Liberman, L.M., Reeves, G.T., Stathopoulos, A., 2009. Quantitative imaging of the Dorsal
588 nuclear gradient reveals limitations to threshold-dependent patterning in Drosophila. Proc Natl
589 Acad Sci U S A 106, 22317-22322.
590 Lim, B., Levine, M., Yamazaki, Y., 2017. Transcriptional Pre-patterning of Drosophila
591 Gastrulation. Curr Biol 27, 610.
592 Morisato, D., Anderson, K.V., 1994. The spatzle gene encodes a component of the
593 extracellular signaling pathway establishing the dorsal-ventral pattern of the Drosophila
594 embryo. Cell 76, 677-688.
595 Nellen, D., Burke, R., Struhl, G., Basler, K., 1996. Direct and long-range action of a DPP
596 morphogen gradient. Cell 85, 357-368.
597 Rahimi, N., Averbukh, I., Haskel-Ittah, M., Degani, N., Schejter, E.D., Barkai, N., Shilo, B.Z.,
598 2016. A WntD-Dependent Integral Feedback Loop Attenuates Variability in Drosophila Toll
599 Signaling. Dev Cell 36, 401-414.
600 Reversade, B., De Robertis, E.M., 2005. Regulation of ADMP and BMP2/4/7 at opposite
601 embryonic poles generates a self-regulating morphogenetic field. Cell 123, 1147-1160.
602 Rusch, J., Levine, M., 1996. Threshold responses to the dorsal regulatory gradient and the
603 subdivision of primary tissue territories in the Drosophila embryo. Curr Opin Genet Dev 6,
604 416-423.
605 Schneider, D.S., Jin, Y., Morisato, D., Anderson, K.V., 1994. A processed form of the Spatzle
606 protein defines dorsal-ventral polarity in the Drosophila embryo. Development 120, 1243-
607 1250.
608 Shilo, B.Z., Barkai, N., 2017. Buffering Global Variability of Morphogen Gradients. Dev Cell
609 40, 429-438.
610 Shilo, B.Z., Haskel-Ittah, M., Ben-Zvi, D., Schejter, E.D., Barkai, N., 2013. Creating gradients
611 by morphogen shuttling. Trends Genet 29, 339-347.
612 Shimmi, O., Umulis, D., Othmer, H., O'Connor, M.B., 2005. Facilitated transport of a
613 Dpp/Scw heterodimer by Sog/Tsg leads to robust patterning of the Drosophila blastoderm
614 embryo. Cell 120, 873-886.
615 Stein, D., Roth, S., Vogelsang, E., Nusslein-Volhard, C., 1991. The polarity of the dorsoventral
616 axis in the Drosophila embryo is defined by an extracellular signal. Cell 65, 725-735.

617 Tanimoto, H., Itoh, S., ten Dijke, P., Tabata, T., 2000. Hedgehog creates a gradient of DPP
618 activity in Drosophila wing imaginal discs. Mol Cell 5, 59-71.
619 Trcek, T., Lionnet, T., Shroff, H., Lehmann, R., 2017. mRNA quantification using single-
620 molecule FISH in Drosophila embryos. Nat Protoc 12, 1326-1348.
621 van der Zee, M., Stockhammer, O., von Levetzow, C., Nunes da Fonseca, R., Roth, S., 2006.
622 Sog/Chordin is required for ventral-to-dorsal Dpp/BMP transport and head formation in a short
623 germ insect. Proc Natl Acad Sci U S A 103, 16307-16312.
624 Wang, Y.C., Ferguson, E.L., 2005. Spatial bistability of Dpp-receptor interactions during
625 Drosophila dorsal-ventral patterning. Nature 434, 229-234.
626 Weber, A.N., Tauszig-Delamasure, S., Hoffmann, J.A., Lelievre, E., Gascan, H., Ray, K.P.,
627 Morse, M.A., Imler, J.L., Gay, N.J., 2003. Binding of the Drosophila cytokine Spatzle to Toll
628 is direct and establishes signaling. Nat Immunol 4, 794-800.
629 Wolpert, L., 1971. Positional information and pattern formation. Curr Top Dev Biol 6, 183-
630 224.
631 Wotton, K.R., Alcaine-Colet, A., Jaeger, J., Jimenez-Guri, E., 2017. Non-canonical
632 dorsoventral patterning in the moth midge Clogmia albipunctata. Evodevo 8, 20.
633 Zhang, Y., Yu, J.C., Jiang, T., Fernandez-Gonzalez, R., Harris, T.J.C., 2018. Collision of
634 Expanding Actin Caps with Actomyosin Borders for Cortical Bending and Mitotic Rounding
635 in a Syncytium. Dev Cell 45, 551-564 e554.
636

637

638 # Figure Legends

639 **Figure 1. Dynamics of Dl-nuclear localization.** (A) Schematic cross-section of an early
640 embryo: Spz is distributed in a sharp gradient along the D-V axis within the peri-vitaline
641 space. Spz binding to the Toll receptor triggers a signaling cascade, culminating in a gradient
642 of nuclear Dl with a sharp ventral peak. Generation of the Spz sharp gradient was proposed to
643 employ a self-organized shuttling mechanism (Haskel-Ittah et al., 2012). (B) A frame from a
644 Light Sheet time-lapse movie following the dynamics of endogenously expressed Dl-GFP in
645 the entire embryo. The gradient can be visualized already at NC 12, it is lost during nuclear
646 divisions and is re-generated at the onset of each nuclear cycle. (C) Each frame of the 3D Light
647 Sheet scan was projected to a 2D map using the ImSAnE tool (Heemskerk and Streichan,
648 2015). Here, the 2D projection of the frame from B is shown. The quantification of Dl-GFP
649 intensity in the nuclei along the D-V axis at 1 min intervals was carried out on nuclei inside the
650 dashed frame. This region, which is close to the middle of the A-P axis, is not distorted by the
651 2D projection (See Methods). (D) Dl-GFP intensity, plotted as function of relative location
652 along the D-V axis (relative location axis x/L is defined as location divided by embryo
653 circumference (See Methods)). A curve is shown for each time point for NC 12, 13 and 14 for
654 the same *wt* embryo. Each Dl-GFP intensity curve was smoothened and normalized by the
655 maximal value attained during NC14 (See Methods). Time points are one minute apart, going
656 from earliest time points in blue to the latest in red. Duration of each NC in minutes is
657 indicated above the plot.

658 **Figure 2. Measured nuclear Dl dynamics during NC14 indicates ongoing shuttling.** (A-D)
659 Measured nuclear Dl temporal dynamics for a *wt* embryo, time points are color coded and are
660 one minute apart. (E-P) Simulations of nuclear Dl temporal dynamics (See SI). (E-H)
661 Diffusion model: nuclear Dl localization induced by Spz binding the Toll receptor, with Spz
662 diffusing out of a wide source while being degraded. (I-L) Constant external gradient model:
663 nuclear Dl localization induced by Spz binding the Toll receptor, with a Spz gradient that is
664 constant in time. (M-P) Full model: nuclear Dl localization induced by Spz binding the Toll
665 receptor, with shuttling of Spz. (A,E,I,M) Nuclear Dl levels in [a.u], plotted as function of
666 relative location along the D-V axis. A curve is shown for each time point, time points are

667 color coded. (B,F,J,N) Nuclear Dl levels at specific locations along the D-V axis, as function of
668 time. Nuclear localizations along the D-V axis are color coded. Each location's curve was
669 normalized by its own maximal value. (C,G,K,O) Nuclear Dl temporal derivative at specific
670 locations along the D-V axis, as function of time. Each location's curve was normalized by its
671 own maximal value. (D,H,L,P) Nuclear Dl temporal derivative at specific locations along the
672 D-V axis, as function of nuclear Dl. Each location's curve was normalized by its own maximal
673 value. Color codes for the location of nuclei along the D-V axis and for the temporal dynamics
674 are shown.

675 **Figure 3. Shuttling dynamics are impaired in the absence of WntD**. (A) A scheme showing
676 the integral feed-back loop between Dl and WntD. *wntD* expression is restricted to the
677 posterior side of the embryo (purple) and is induced by Dl. (B) A scheme showing WntD
678 binding to Fz4, and restricting the binding of Spz to the Toll receptor. (C,F) Simulations of Dl
679 temporal dynamics in the full model for a *wt* (C) and *wntD* mutant (F) embryo (See SI). Time
680 points are color coded. For the *wntD* mutant, the double peak is more prominent and does not
681 fully converge resulting in a flat peak. (D,G) Measured Dl temporal dynamics for a *wt* (D) and
682 *wntD* mutant (G) embryo (See Methods). Time points are color coded, and are one minute
683 apart. As predicted by the model, the *wntD* mutant exhibits less efficient shuttling leading to a
684 more prominent double peak, which does not fully converge, resulting in a flat peak. (E,H) Log
685 of Dl-GFP intensity temporal dynamics at selected locations along the D-V axis for a *wt* (E)
686 and *wntD* mutant (H) embryo from panels D,G. Locations are color coded. Measured values
687 were background subtracted and smoothed in time (See Methods). The flat peak of the *wntD*
688 mutant embryo results in very similar Dl values over time for the four ventral most curves,
689 while in the *wt* embryo each curve attains a different final value and has different dynamics.
690 (I-J) Peak sharpness over time (calculated as std/mean in % of values close to the peak, See
691 Methods) in a population of *wt* embryos (black) and *wntD* mutant embryos (red) during NC 13
692 (I) and NC14 (J). Bold lines indicate population mean and surrounding color indicates standard
693 error. Number of embryos in each population is indicted in plot. Sharpness in the *wt* population
694 increases over time to a value significantly higher than the *wntD* mutant population. The *wntD*
695 mutant population exhibits an initial increase in peak sharpness due to the prominent double
696 peak, followed by a decrease due to peak flattening. (K) Scheme showing the global

697 attenuation effect of WntD on Toll availability, leading to redirection of active ligand binding
698 towards more ventral positions. (L) In *wntD* mutants additional Toll receptors become
699 available, leading to increased ligand binding in lateral regions, generating a flatter peak of
700 signaling.

701 **Figure 4. An enlarged ventral furrow is formed in the absence of WntD.** Snapshots of
702 cross-sections of a *wt* (A-D) vs. *wntD* mutant embryo (E-F) expressing Dl-GFP, showing the
703 ventral nuclei during NC 14. Time in NC 14 (in minutes) is indicated. When the first sign of
704 invagination appeared, the most lateral nuclei still displaying positional change were marked
705 (yellow). Working backwards in the movies allowed an accurate count of the nuclei between
706 them prior to invagination.

707 **Figure 5. Dynamics of *wntD* transcription**. (A) Schematic representation of the *wntD*::MS2
708 reporter. The 1.2 kb regulatory region upstream of the *wntD* coding sequence drives the
709 expression of Fhos-RH with 24 MS2 repeats located at its 5' end. (B) Light Sheet live imaging
710 of the transcriptional activity of the *wntD* promoter enables a quantitative analysis of its
711 dynamics. Embryos express His:RFP which marks nuclei in red and the transcriptional activity
712 is indicated by the green signal. (B-F) A constant reduction in the number of nuclei expressing
713 *wntD* is observed from NC12 onwards, such that by NC 14 no transcription is observed. Since
714 the *wntD* promoter responds to the level of Dl, we assume that this reduction reflects the
715 attenuating activity of WntD.

716 **Figure 6. Graded accumulation of T48 transcripts is driven by the dynamics of Dl-**
717 **nuclear entry.** (A) Time lapse images from the beginning of NC 14, showing the dynamics of
718 the onset of *T48* transcription in a *wt* embryo, followed by *T48*::MS2. Nuclei displaying
719 transcription were highlighted in yellow. Arrows mark the edges of the domain at each time
720 point. (B) Quantification of the data in (A). Times are color-coded according to (A), Y axis
721 represents the normalized number of transcription start sites (TSs) along the A-P axis, X axis
722 represents the position along the D-V axis. (C) The intensity of *T48*::MS2 signal for nuclei
723 across the D-V axis at 33 min. Once *T48* transcription is initiated, it progresses at comparable
724 rates in all nuclei. (D,E) Single molecule FISH for *T48* showing the intensity of transcription
725 and the number of active nuclei across the region expressing *T48*. Nuclei are marked by DAPI

726 (blue) and *T48* probe in red. Once transcription is initiated it proceeds at a similar rate by all
727 nuclei, and the number of nuclei expressing *T48* in ventral and ventro-lateral regions is
728 comparable. (F) The ventral *T48* expression domain, arrows mark TSs. (G) Quantification of
729 smFISH data: Number of *T48* mRNA molecules in black bars, and TSs intensity corresponding
730 to transcription rate in blue diamonds.

731 **Figure 7. Dynamics of Spz shuttling establishes pattern.** The shuttling mechanism operates
732 within a wide domain D-V predefined by Pipe expression during oogenesis. Initially, a double-
733 peak distribution of the Spz morphogen in the peri-vitelline space is observed. In *wt* embryos
734 shuttling operates efficiently to concentrate the Spz morphogen to a single sharp peak. The
735 dynamics of the Dl gradient are utilized by the embryo to induce graded accumulation of *T48*
736 transcripts, which facilitate recruitment of RhoGEF2 and ultimately Rho1 and actomyosin, to
737 drive apical constriction of invaginating mesodermal cells. Loss of WntD renders shuttling less
738 efficient, leading to a flattened peak of morphogen distribution. This may result in impaired
739 distribution of *T48* transcripts and therefore in a broader gastrulation furrow.
740

741 Figure 1

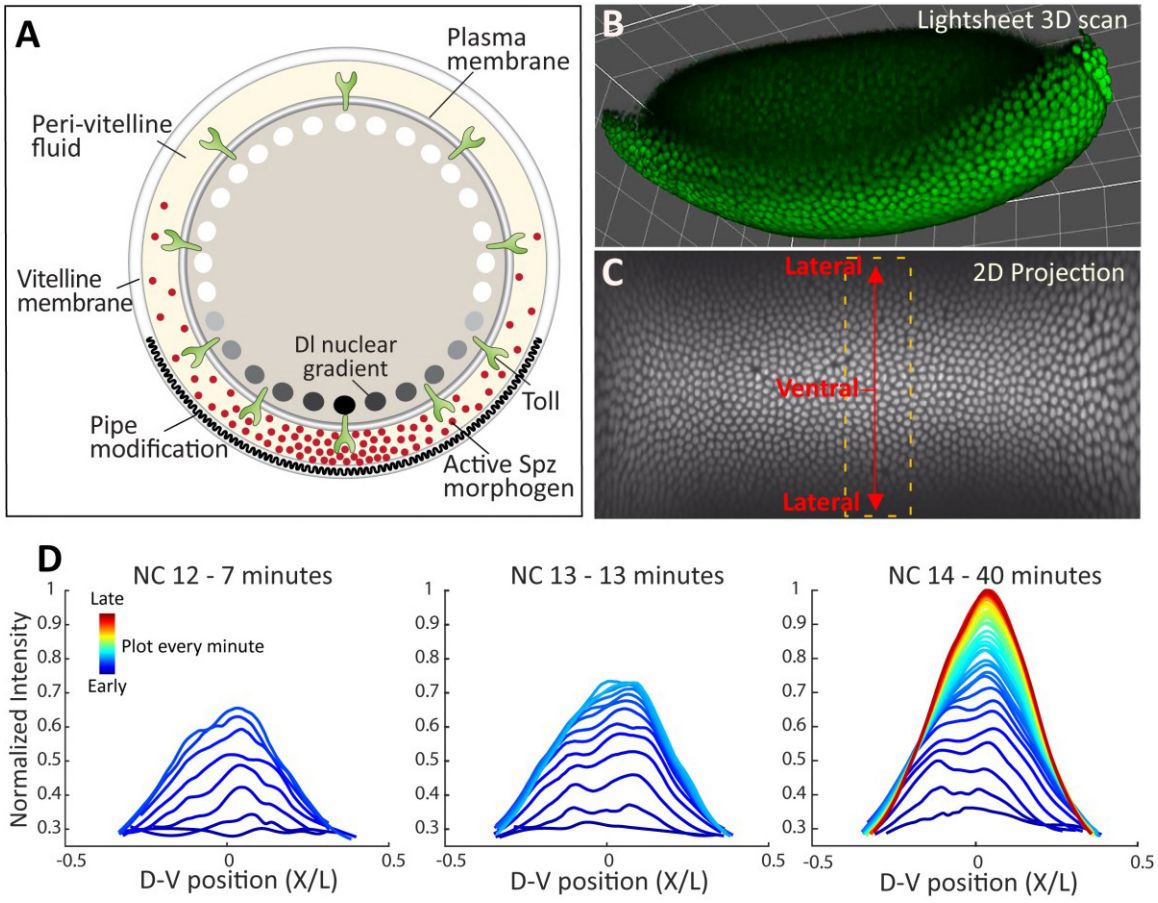

742

743

744

Figure 2

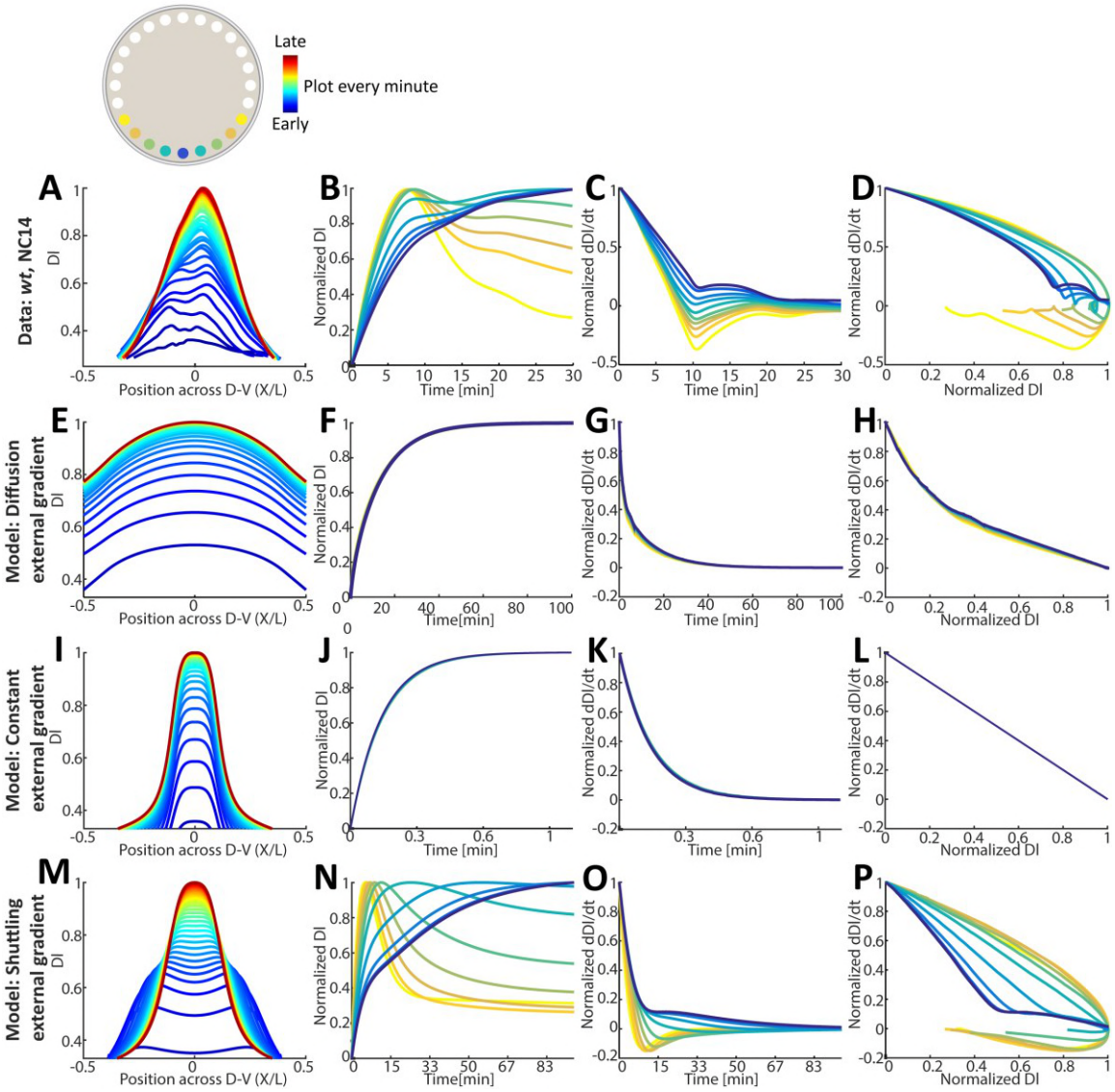
Late
Plot every minute
Early
A
B
C
D
Data: wt, NC14
DI
Position across D-V (X/L)
Normalized DI
Time [min]
Normalized dDI/dt
E
F
G
H
Model: Diffusion external gradient
Time[min]
I
J
K
L
Model: Constant external gradient
M
N
O
P
Model: Shuttling external gradient

Figure 3

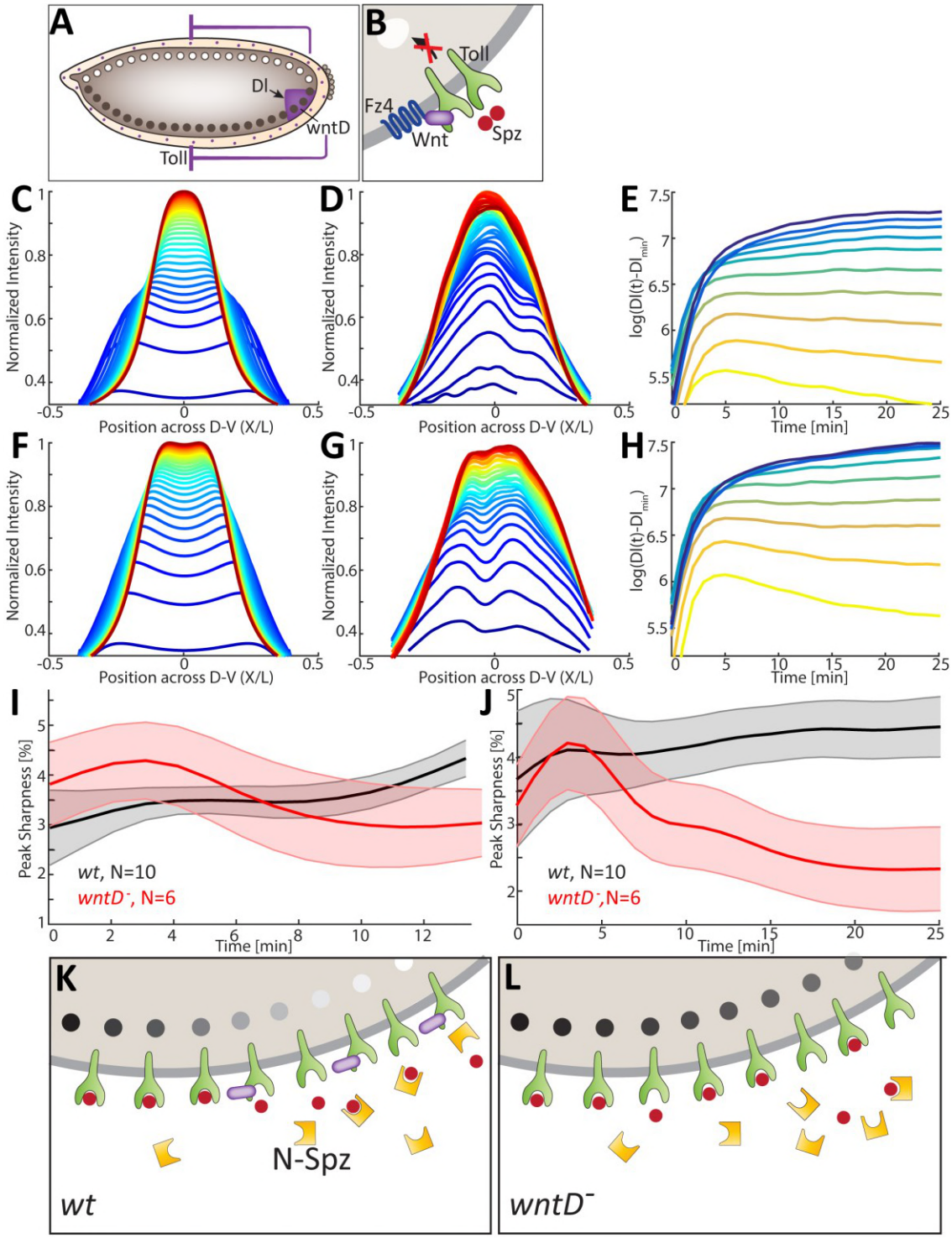
A
Dl
wntD
Toll
B
Toll
Fz4
Wnt
Spz
C
D
E
F
G
H
Normalized Intensity
Position across D-V (X/L)
log(Dl(t)-Dl_min)
Time [min]
I
J
Peak Sharpness [%]
wt, N=10
wntD⁻, N=6
K
L
N-Spz
wt
wntD⁻

751 Figure 4

752

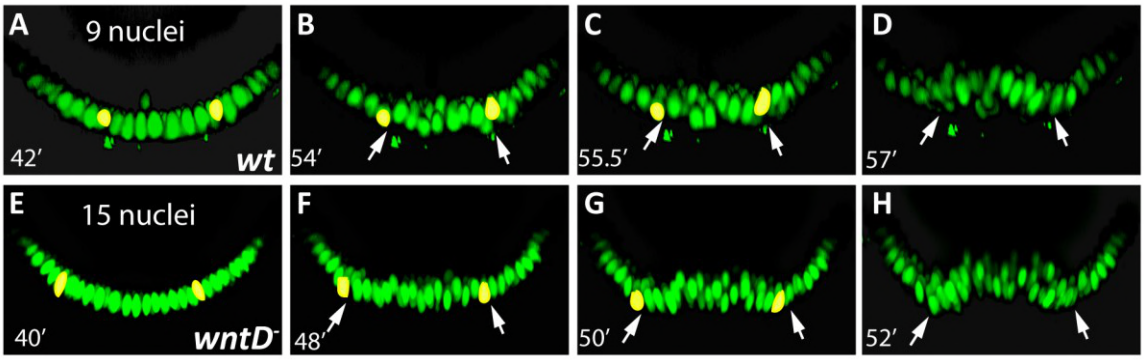

753

754

755 Figure 5

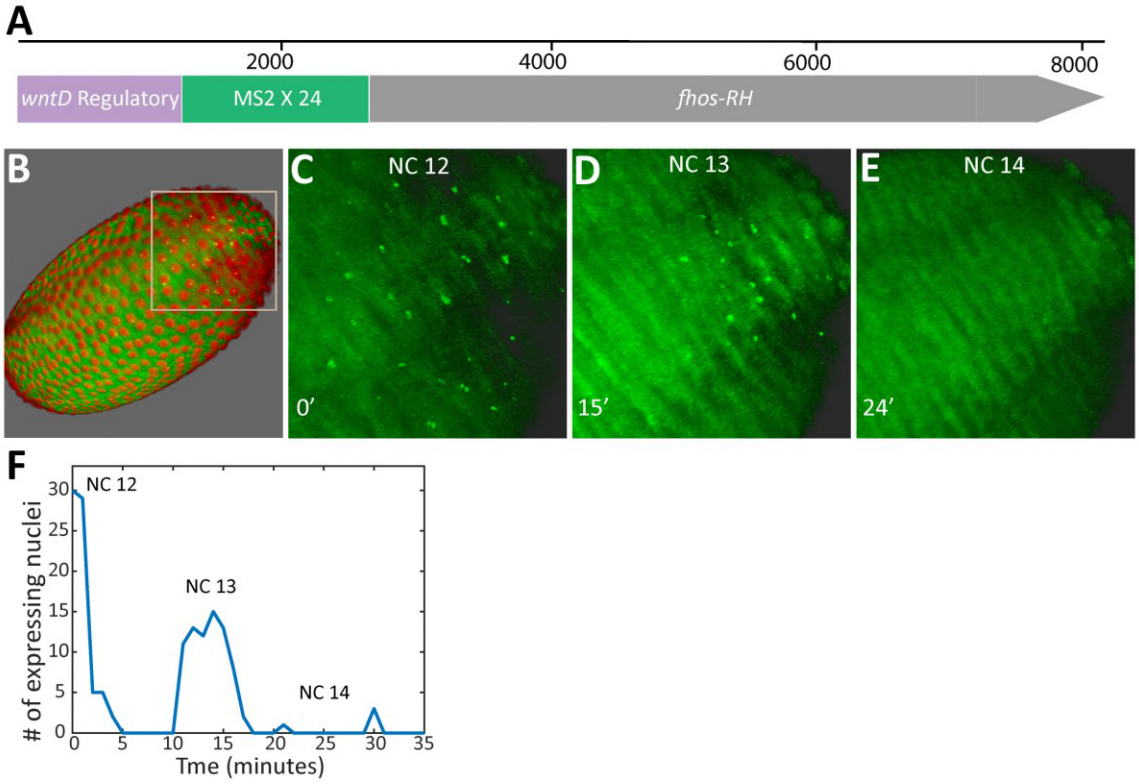

756

757

758 Figure 6

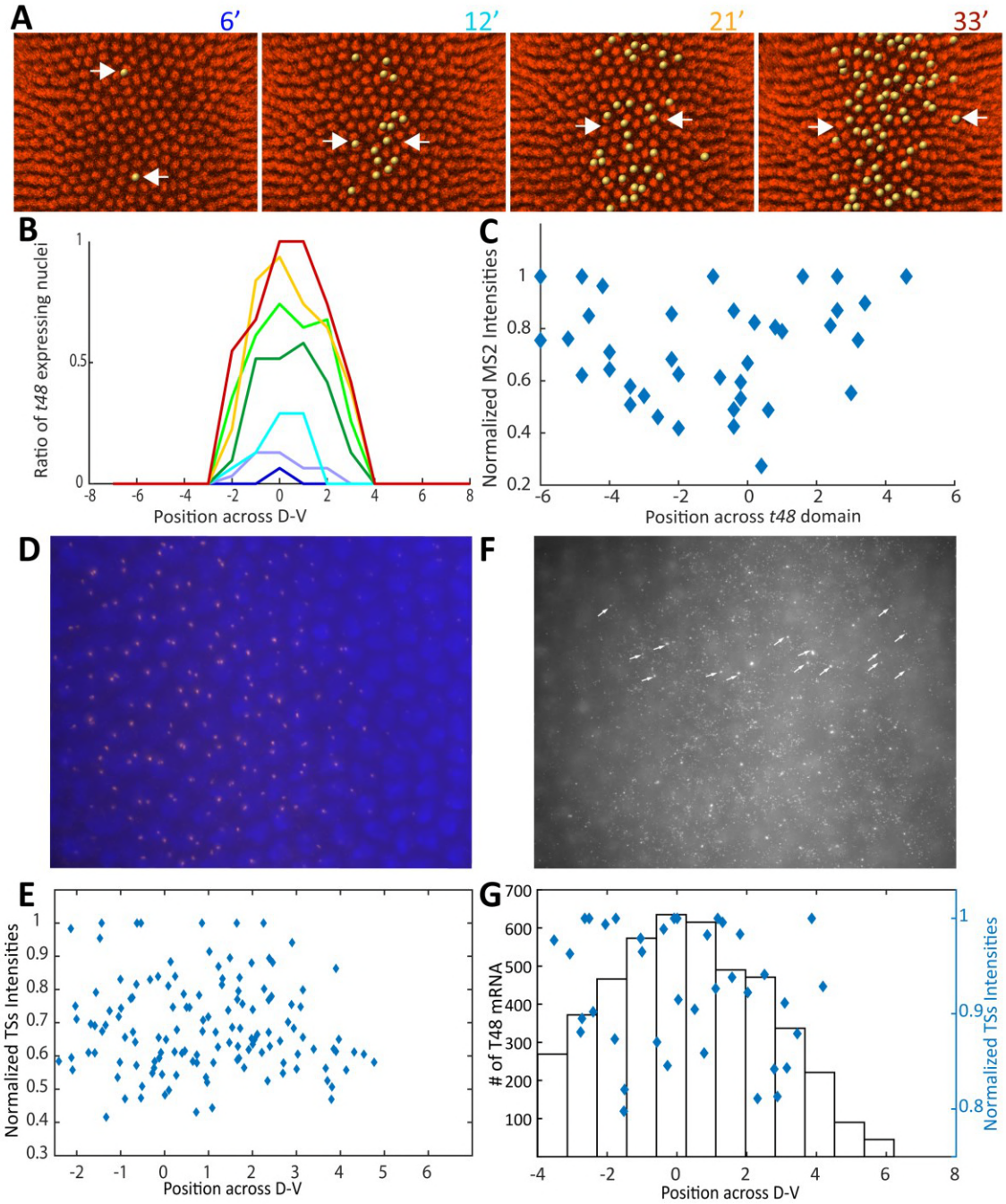

759

760

761 Figure 7

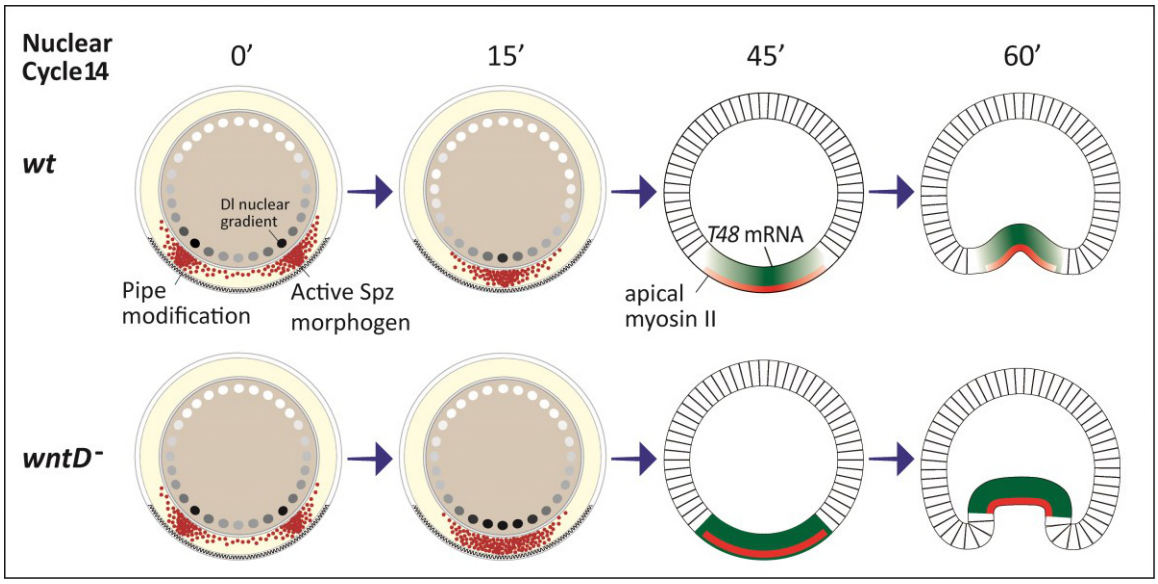

762

763

Dynamics of Spaetzle morphogen shuttling in the *Drosophila* embryo shapes pattern

Supplemental Information

Contents

Supplemental Movies, figures and Tables 35
Mathematical model 39
Full model equations 40
Full model parameters 41
Constant external gradient model 41
Naïve diffusion model 42
Shuttling parameters effect on double peak prominence 42
References 43

Supplemental Movies, figures and Tables

Movie 1 - A Light Sheet time-lapse movie following the dynamics of endogenously expressed Dl-GFP in the entire embryo. The nuclear Dl gradient can be seen in nuclei at the ventral side (bottom) already at NC 12, it is lost during nuclear divisions and is re-generated at the onset of each nuclear cycle.

Movie 2 - A frame by frame 2D projection of movie 1 done using the ImSAnE tool (Heemskerk and Streichan, 2015). Dl-GFP appears in grey.

Movie 3 - Time lapse of Dl-GFP intensity data for the area inside the dashed frame in Figure 1C. Each circular marker in the movie shows raw, non smoothed Dl-GFP intensity in a single nucleus. Nuclei were segmented from the corresponding frames of movie 2 (See Methods).

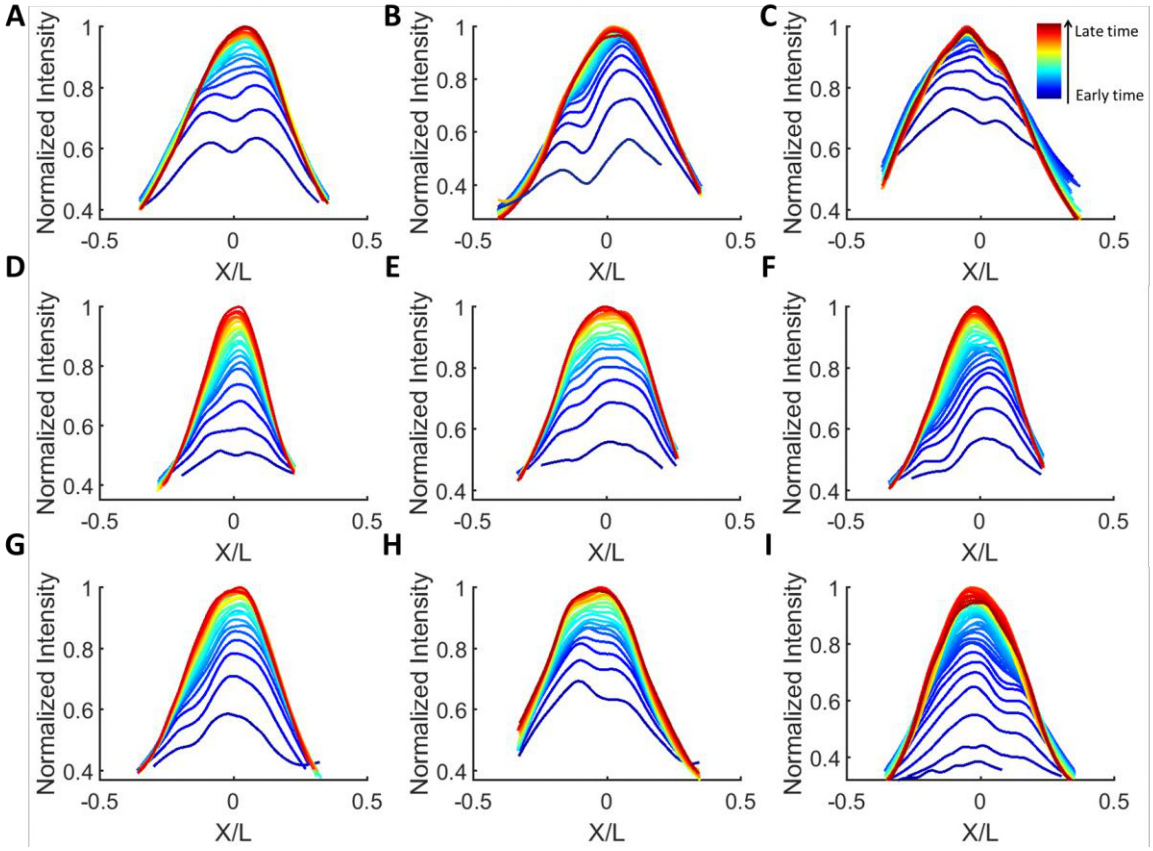

Figure S1 – Dl temporal dynamics during NC14 in *wt* embryos. Dl-GFP intensity, plotted as function of relative location along the DV axis, relative location axis x/L is defined as location divided by embryo circumference (See Methods). A curve is shown for each time point during NC14 for 9 *wt* embryos. Each Dl-GFP intensity curve was smoothened and normalized by the maximal value attained during NC14 (See Methods). Time points are 1.5 minutes apart for (A-H) and 1 minute apart for I, going from earliest time points in blue to the latest in red. All embryos exhibit shuttling signatures: lateral overshoots and converging double peaks.

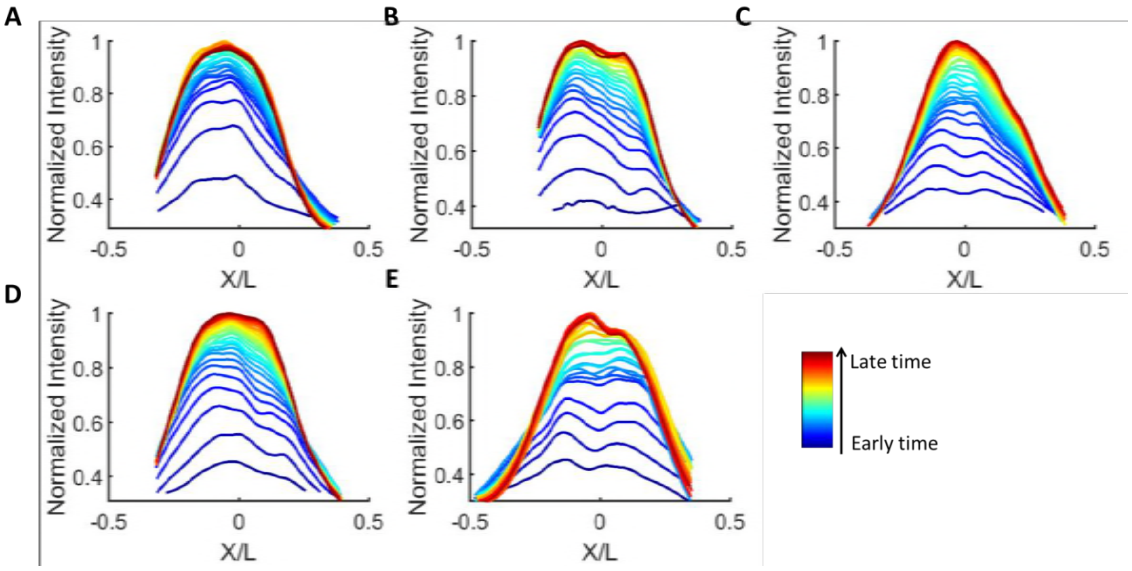

Figure S2 - Dl temporal dynamics during NC14 in *wntD-/-* embryos. Dl-GFP intensity, plotted as function of relative location along the DV axis, relative location axis x/L is defined as location divided by embryo circumference (See Methods). A curve is shown for each time point during NC14 for 5 *wntD-/-* embryos. Each Dl-GFP intensity curve was smoothened and normalized by the maximal value attained during NC14 (See Methods). Time points are 1.5 minutes apart for, going from earliest time points in blue to the latest in red. All embryos exhibit shuttling signatures: lateral overshoots and double peaks flattening over time.

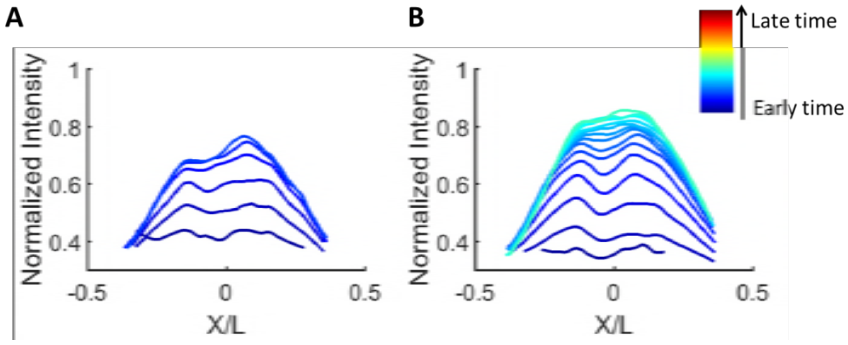

Figure S3 - Dl temporal dynamics during NC12-13 in a *wntD-/-* embryo. Dl-GFP intensity, plotted as function of relative location along the DV axis, relative location axis x/L is defined as location divided by embryo circumference (See Methods). A curve is shown for each time point during NC12 (A) and NC13 (B) for the *wntD-/-* embryo presented in Figure 3E. Each Dl-GFP intensity curve was smoothened and normalized by the maximal value attained during NC14 (See Methods, Figure 3E). Time points are 1 minute apart for, going from earliest time points in blue to the latest in red.

Table S1 : Parameters table for full model, WT values

#	Parameter	Units type	Meaning	Value in a.u	Units	Value in units
1	K_{rec}	t^{-1}	Toll receptor recycling rate	0.07	$\sec^{-1}$	0.007
2	K_{end}	t^{-1}	Toll receptor endocytosis rate	1	$\sec^{-1}$	0.1
3	λ	t^{-1}	NCSpz* cleavage rate	4.2	$\sec^{-1}$	0.42
4	α_N	t^{-1}	NSpz degradation rate	0.0011	$\sec^{-1}$	0.00011
5	α_c	t^{-1}	CSpz degradation rate	0.0014	$\sec^{-1}$	0.00014
6	α_{Nc}	t^{-1}	NCSpz degradation rate	0.0016	$\sec^{-1}$	0.00016
7	$K_{on,c}$	$t^{-1}C$	CSpz binding to Toll	0.3	$\mu M\sec^{-1}$	0.0013
8	$K_{off,c}$	$t^{-1}C$	CSpz un-binding from Toll	1.12	$\mu M\sec^{-1}$	0.0049
9	K_{on}	$t^{-1}C$	NCSpz binding to Toll	0.008	$\mu M\sec^{-1}$	3.2e-5
10	K_{off}	$t^{-1}C$	NCSpz un-binding from Toll	0.1	$\mu M\sec^{-1}$	4.33e-04
11	η_0	$t^{-1}C$	NCSpz activation rate	0.22	$\mu M\sec^{-1}$	9.68e-4
12	K_{bind}	$t^{-1}C$	CSpz binding rate to NSpz	7	$\mu M\sec^{-1}$	0.0308
13	K_{split}	t^{-1}	NC-Tl splitting rate to C-Tl and 2*N-Spz , on Toll	10	$\sec^{-1}$	1
14	D_{NC}	x^2t^{-1}	NCSpz diffusion coefficient	0.1186	$\mu m^2\sec^{-1}$	118.6
15	D_N	x^2t^{-1}	NSpz diffusion coefficient	0.0055	$\mu m^2\sec^{-1}$	55
16	D_{NC*}	x^2t^{-1}	NCSpz* diffusion coefficient	0.745	$\mu m^2\sec^{-1}$	745
17	T_{tot}	C	Total Toll level	5.625	μM	0.25
18	D_W	x^2t^{-1}	WntD diffusion coefficient	0.5	$\mu m^2\sec^{-1}$	500
19	α_w	t^{-1}	WntD degradation rate	0.001	$\sec^{-1}$	1.4e-5
20	β_w	$t^{-1}C$	WntD production rate	0.1	$\mu M\sec^{-1}$	4.4e-4
21	K_w	C^{n_w}	K_D of WntD production as a function of signaling	9e-10	μM^{n_w}	4.7e-30
22	n_w	-	Hill coefficient of WntD production as a function of signaling	15	-	15
23	L	x	Length of tissue	2	μm	250

24	X_{pipe}	%	% of L below which a point $\vec{x} = (x, y, z) \in pipe\ domain$	40	%	40
25	X_{WntD}	%	% of L above which a point $\vec{x} = (x, y, z) \in WntD\ producing\ domain$	25	%	25
26	W_{lower}	%	Maximal lowering of Tl property by WntD	60	%	60
27	W_{Tr}	$C^{n_{lower}}$	K_D of WntD lowering receptor property	5	$\mu M^{n_{lower}}$	0.01
28	n_{lower}	-	Hill coefficient of WntD lowering receptor property	2	-	2
29	T	t	# of discrete time points the simulation was run	600	sec	6000 (~1.5 hours)
30	$K_{Dl,in}$	$t^{-1}C$	Rate of Dl entry into the nucleus	0.07	$\mu M \sec^{-1}$	2.8e-04
31	$K_{Dl,out}$	$t^{-1}C$	Rate of Dl exit from the nucleus	2	$\mu M \sec^{-1}$	0.008
32	Dl_0	C	Initial Dl concentration in the nuclei	1e-4	μM	4.4e-06
33	Dl_{tot}	C	Total amount of Dl	5	μM	0.22

Mathematical model

Our full model describes how the Spz gradient is formed by shuttling, induces the nuclear localization of Dl and the negative feedback between WntD and Dorsal which maintains the gradients robustness (Rahimi et al., 2016). To this end, we extend the model from our previous paper (Rahimi et al., 2016) to include the nuclear localization of Dorsal. Also, we used a different mechanism by which WntD contracts the Spz gradient: instead of competing with the ligand for binding the Toll receptor, we assume here that WntD "crowds" the Toll receptors immediate environment by binding its own receptor Frizzled4 and limiting the access of Spz to Toll. This increases the chances of free ligand binding the shuttling molecule instead of the receptor and therefore enhances shuttling. This "crowding" of Toll has an additional affect: stabilizing the ligand which succeeded in binding, which also makes shuttling more efficient.

The governing set of reaction-diffusion equations of our model is given below: **eqn. 1** defines the temporal dynamics of freely diffusing WntD. The terms of the equation by order of appearance describe: WntD diffusion, WntD degradation, WntD production which depends on nuclear Dorsal. This last term is the induction part of InC as WntD production is positively regulated by signaling. The WntD producing zone is restricted and is defined in the embryo by the Torso signaling border. In the simulations we define this zone using the model parameter X_{WntD}: WntD production is only allowed for points posterior to X_{WntD} . **Eqn. 2** defines the nonlinear saturating function $R_w(\vec{x}, t)$ through which WntD changes the properties of the Toll receptor: the rate at which ligands bind and unbind from it. **Eqn. 3** defines the temporal dynamics of free Toll receptors. This equation introduces the following constraint: the total amount of Toll receptors (free, bound by ligand and endocytosed) is constant and equals T_{tot}. **Equations 4-10** are the self-organized shuttling model (SOSH) equations as appear in (Haskel-Ittah et al., 2012), we'll review SOSH and the equations briefly. The SOSH mechanism depends on the versatility of the *Spz* protein. The separate inhibitor domain N-Spz and activating region of *Spz,* C-Spz, generated after cleavage of the NC-Spz precursor (**eqn. 4**), can interact with each other in three different modes. These modes facilitate a process of "self-organized shuttling", where the active ligand C-Spz is shuttled and concentrated at the ventral-most region giving rise to the sharp activation gradient of *Toll*. Equations 5-7 describe the shuttling of the active C-Spz ligand (which cannot diffuse on its own) by the N-Spz inhibitor when bound together as the NC-Spz* complex. Signaling occurs when C-Spz bound to Toll

undergoes endocytosis (**eqns. 5,8,10**). Toll receptors undergo recycling back to the membrane after endocytosis and the total concentration of Toll is constant (**eqns. 10,3** respectively). The C-Spz ligand and N-Spz inhibitor are products of NC-Spz complex separation when bound to the Toll receptor (**eqn. 4,9**). NC-Spz is also capable of inducing Toll endocytosis when binding it and thus contributing to signaling (**eqn. 9**) but signaling through NC-Spz happens at a much lower rate than C-Spz mediated signaling. **Equations 11-12** describe the induction of Dorsal nuclear localization by Toll signaling. **Eqn. 11** introduces the following constraint: the total amount of Dorsal (Nuclear- Dl_{in} and cytoplasmic- Dl_{out}) is constant and equals Dl_{tot}. The meaning of the different parameters and their units are summarized in Table S1. This set of equations was solved numerically in 1D using a standard MATLAB PDE solver.

Full model equations

$$(\mathbf{1})\ \frac{\partial[W]}{\partial t} = D_W \nabla^2[W] - \alpha_w[W] + \beta(\vec{x})\frac{[Dl_{in}]^{n_w}}{K_w + [Dl_{in}]^{n_w}}$$

$$\beta(\vec{x}) = \begin{cases} if\ x > X_{WntD} \rightarrow \vec{x} = (x,y,z) \in wntD\ expression\ zone, & \beta_w \\ else, & 0 \end{cases}$$

$$(2)\ R_w(\vec{x},t) = W_{lower} + (1 - W_{lower})\frac{W_{Tr}}{W_{Tr} + [W(\vec{x},t)]^{n_{lower}}}$$

$$(\mathbf{3})\ T_{tot} = [Tl] + [CSpz - Tl] + [NCSpz - Tl] + [Tl_{end}] \rightarrow$$

$$[Tl]_{(\vec{x},t)} = T_{tot} - [CSpz - Tl] - [NCSpz - Tl] + [Tl_{end}]$$

$$(\mathbf{4})\ \frac{\partial[NCSpz]}{\partial t} =$$

$$D_{NC}\nabla^2[NCSpz] - \alpha_{NC}[NCSpz] + \eta(\vec{x}) - R_w K_{on}[Tl][NCSpz] + R_w K_{off}[NCSpz - Tl])$$

$$\eta(\vec{x}) = \begin{cases} if\ \vec{x} = (x,y,z) \in pipe\ domain, & \eta_0 \\ else, & 0 \end{cases}$$

$$(\mathbf{5})\ \frac{\partial[CSpz]}{\partial t} =$$

$$-\alpha_C[CSpz] - R_w K_{on,c}[Tl][CSpz] + R_w K_{off,c}[CSpz - Tl] - K_{bind}[NSpz][CSpz] +$$

$$K_{split}[NCSpz - Tl] + \frac{\lambda\eta(\vec{x})}{\eta_0}[NCSpz *]$$

$$(\mathbf{6})\ \frac{\partial[NSpz]}{\partial t} = D_{NC}\nabla^2[NSpz] - \alpha_{NC}[NSpz] - K_{bind}[NSpz][CSpz] + 2K_{split}[NCSpz - Tl]$$

$$(\mathbf{7})\ \frac{\partial[NCSpz*]}{\partial t} = D_{NC*}\nabla^2[NCSpz *] - \frac{\lambda\eta(\vec{x})}{\eta_0}[NCSpz *] + K_{bind}[NSpz][CSpz]$$

$$(\mathbf{8})\frac{\partial[CSpz-Tl]}{\partial t} = R_w[Tl][CSpz] - R_w K_{off,c}[CSpz-Tl] + K_{split}[NCSpz-Tl] - K_{end}[CSpz-Tl]$$

$$(\mathbf{9})\frac{\partial[NCSpz-Tl]}{\partial t} = R_w K_{on}[Tl][NCSpz] - (R_w K_{off} + K_{split} + K_{end})[NCSpz-Tl]$$

$$(\mathbf{10})\frac{\partial[Tl_{end}]}{\partial t} = K_{end}([CSpz-Tl] + [NCSpz-Tl]) - K_{rec}[Tl_{end}]$$

$$(\mathbf{11})[Dl_{Tot}] = [Dl_{in}] + [Dl_{out}]$$

$$(\mathbf{12})\frac{\partial[Dl_{in}]}{\partial t} = K_{Dl,in}[Tl_{end}][Dl_{out}] - K_{Dl,out}[Dl_{in}]$$

Full model parameters

When choosing parameters, we relied on our previous papers where SOSH (Haskel-Ittah et al., 2012) and InC (Rahimi et al., 2016) were previously analyzed. For the SOSH WT parameters we in this work, we used the SOSH parameter values described in Table S5 of (Haskel-Ittah et al., 2012) with slight alterations to better resemble our experimental data. Values for WntD related parameters (diffusion, degradation, and production rates) were based on our previous paper (Rahimi et al., 2016). The addition of Dorsal nuclear localization (eqns. 11-12) introduced new dorsal related parameters, which were selected to resemble similar parameters in the model (for example, the total concentration of Dorsal is similar to that of Toll). For the simulation of WntD mutants, model equations were solved with the WntD production rate set to zero.

Constant external gradient model

In order to simulate only Dorsal nuclear localization induced by a constant Toll signaling profile, the following set of equations was solved:

$$(\mathbf{13})\frac{\partial[Tl_{end}]}{\partial t} = 0, \qquad [Tl_{end}] = Tl_{end}^{final}(X)$$

$$(\mathbf{14})[Dl_{Tot}] = [Dl_{in}] + [Dl_{out}]$$

$$(\mathbf{15})\frac{\partial[Dl_{in}]}{\partial t} = K_{Dl,in}[Tl_{end}][Dl_{out}] - K_{Dl,out}[Dl_{in}]$$

The constant external gradient, Tl_{end}^{final}, was selected to be the sharp Toll signaling profile $[Tl_{end}]$ at the last time point for the simulation of the full model (eqns 1-12). Parameter values according to Table S1.

Naïve diffusion model

This model includes a single ligand, $NCSpz$, which is produced throughout the pipe domain (eqn. 17). The ligand diffuses and is degraded (eqn. 17). It binds the Toll receptor (eqns. 18,16), and induces Dorsal nuclear localization (eqns. 20-21). This model is described by the following equations:

$$\mathbf{(16)}\ T_{tot} = [Tl] + +[NCSpz - Tl] + [Tl_{end}] \rightarrow$$

$$[Tl]_{(\vec{x},t)} = T_{tot} - [NCSpz - Tl] + [Tl_{end}]$$

$$\mathbf{(17)}\ \frac{\partial[NCSpz]}{\partial t} = D_{NC}\nabla^2[NCSpz] - \alpha_{NC}[NCSpz] + \eta(\vec{x}) - K_{on}[Tl][NCSpz] + K_{off}[NCSpz - Tl])$$

$$\eta(\vec{x}) = \begin{cases} if\ \vec{x} = (x,y,z) \in pipe\ domain, & \eta_0 \\ else, & 0 \end{cases}$$

$$\mathbf{(18)}\ \frac{\partial[NCSpz-Tl]}{\partial t} = K_{on}[Tl][NCSpz] - (K_{off} + K_{end})[NCSpz - Tl]$$

$$\mathbf{(19)}\ \frac{\partial[Tl_{end}]}{\partial t} = K_{end}([NCSpz - Tl]) - K_{rec}[Tl_{end}]$$

$$\mathbf{(20)}\ [Dl_{Tot}] = [Dl_{in}] + [Dl_{out}]$$

$$\mathbf{(21)}\ \frac{\partial[Dl_{in}]}{\partial t} = K_{Dl,in}[Tl_{end}][Dl_{out}] - K_{Dl,out}[Dl_{in}]$$

Parameter values according to Table S1. See further analytical and numerical analysis for the sharpness and robustness of the gradient in this model in (Haskel-Ittah et al., 2012).

Shuttling parameters effect on double peak prominence

The prominence of the converging double peak feature in the shuttling model depends on model parameters which control the mean path the shuttling complex travels ventrally before being cleaved, relative to the length of the source (pipe domain). This mean path is influenced by several parameters, mainly tissue absolute length L (when maintaining the source as 40% of absolute length), changing source length directly by assuming the pipe domain is smaller or larger than 40% of the circumference, cleavage rate of the shuttling complex λ, diffusion coefficient of the shuttling complex D_{NC*}. For a sufficiently large ratio

between the mean path and L, no double peak will be observed. Lowering this ratio increases the prominence of the double peak. For a sufficiently small ratio, the double peak does not converge into a single peak since the shuttling complex cannot penetrate all the way to the ventral most. We demonstrate this by solving the full model for our WT parameter set (Table S1), and comparing to sets where these parameters are perturbed: decreased 2 fold and increased 2 fold:

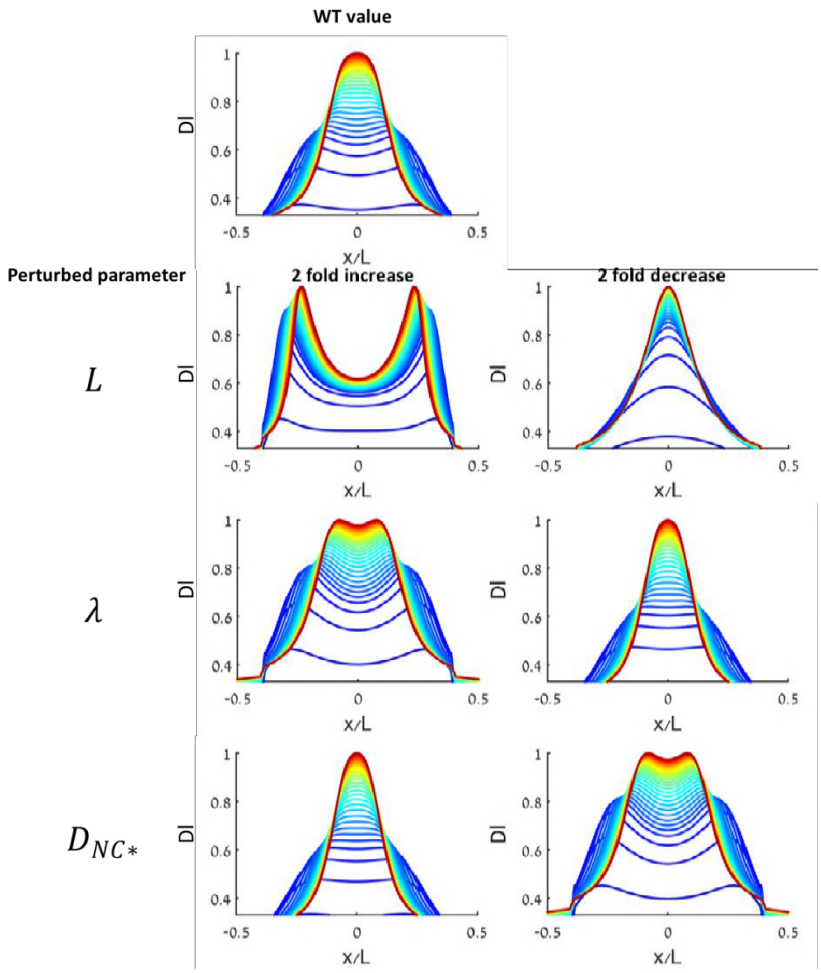

Model Supplement Figure 1 – Perturbations to shuttling complex parameters modulate double peak prominence.

References

Haskel-Ittah, M., Ben-Zvi, D., Branski-Arieli, M., Schejter, E.D., Shilo, B.Z., Barkai, N., 2012. Self-organized shuttling: generating sharp dorsoventral polarity in the early Drosophila embryo. Cell 150, 1016-1028.

Heemskerk, I., Streichan, S.J., 2015. Tissue cartography: compressing bio-image data by dimensional reduction. Nat Methods 12, 1139-1142.

922 Rahimi, N., Averbukh, I., Haskel-Ittah, M., Degani, N., Schejter, E.D., Barkai, N., Shilo, B.Z.,
923 2016. A WntD-Dependent Integral Feedback Loop Attenuates Variability in Drosophila Toll
924 Signaling. Dev Cell 36, 401-414.
925